Electrochemical and Spectro-Microscopic Analyses of Charge Accumulation and Ion Migration in Dry Processed Perovskite Solar Cells under Electrical Biasing

Haeyeon Jun, Denis Tondelier, Bernard Geffroy, Ileana Florea, Jean-eric Bouree, Pilar Lopez-Varo, Philip Schulz, Yvan Bonnassieux, Sufal Swaraj

"This work is intended for submission to ACS Nano."

Electrochemical and Spectro-Microscopic Analyses of Charge Accumulation and Ion Migration in Dry Processed Perovskite Solar Cells under Electrical Biasing

Haeyeon Jun[1,2], Denis Tondelier[2], Bernard Geffroy[2,3], Ileana Florea[4], Jean-Eric Bouree[2], Pilar Lopez-Varo[5], Philip Schulz[2, 5], Yvan Bonnassieux[2]* & Sufal Swaraj[1]*

[1]Synchrotron SOLEIL, L'Orme des Merisiers, Départementale 128, 91190 Saint-Aubin, France
[2]LPICM, CNRS, École Polytechnique, Institut Polytechnique de Paris, Route de Saclay, 91128 Palaiseau, France
[3]Université Paris-Saclay, CEA, CNRS, NIMBE, LICSEN, 91191, Gif-sur-Yvette, France
[4]CRHEA, CNRS, UMR7073, Rue Bernard Grégory, 06905 Sophia-Antipolis Cedex FrancePhilip.SCHULZ@cnrs.fr
[5]IPVF, UMR 9006, 18, Boulevard Thomas Gobert, 91120 Palaiseau

*Email: sufal.swaraj@synchrotron-soleil.fr, yvan.bonnassieux@polytechnique.edu

Keywords: Organic-inorganic metal halide perovskite, ion-migration, STXM, Electrochemical impedance spectroscopy, solar cells, ageing

Abstract: We study the influence of the electrical biasing on the modification of the chemical composition and the electrical performance of perovskite solar cells (PSCs) by coupling Electrochemical impedance spectroscopy (EIS) and scanning transmission X-ray microscopy (STXM) techniques. EIS reveals the formation of charge accumulation at the interfaces and changes in resistive and capacitive properties. STXM study on PSCs after applying strong electric field for a long biasing time indicates the break-down of methylammonium (MA^+) cation promoting iodide ions to migrate and create defects at the interface. This complementary EIS and STXM study allows to suggest a degradation mechanism that includes the migration of iodide ions that leads to interface defects and subsequent degradation of solar cell performance. In addition, we study the evolution of the performance of PSCs under air. We observe an increased hysteresis index on current-voltage curves and fill factor reduction of the perovskite solar cells with ageing in air. EIS measurements show the formation of a capacitive layer resulting from accumulation of iodide ions through modification of the mobile ion concentration and ion mobility.

I. Introduction:

In response to the urgency of climate change and energy crisis several solar cell

technologies are being explored. Organic-inorganic metal halide perovskite solar cells are one of the most promising emerging technologies in the race to achieve the Shocley-Queisser limit efficiency. The application of perovskite materials in solar cell and tandem devices is an active area of research where the focus is primarily on improving the lifetime of these devices while exploiting their optoelectronic properties to the maximum. Despite their rapid rise to 26.1% efficiency for perovskite solar cells (PSC's) and 33.9 % for perovskite/Si tandem cells [1, 2], the low stability of these devices is still hindering their real-world applications.

Intrinsic factors, such as those related to material properties, morphological factors, grain size, crystallinity and extrinsic factors such as exposure to moisture, UV radiation, temperature and voltage biasing have been investigated for their negative impact on the operational lifetime of these materials [3] [4] [5] [6] [7]. To mitigate these drawbacks, architectural and chemical modifications and interface engineering have been explored for these devices [8], [9] [10] [11]. Ageing of these devices under air and humidity has been extensively investigated with most reports discussing the degradation of the PSC's, although some reports of self-enhancement can also be found [12] [13] [14].

One of the factors that remains relatively less explored is the influence of electric field on the degradation of perovskite solar cells [15]. Under operating conditions, the internal electric field on PSCs is constantly modified due to the different photogenerated charge carriers (electrons and holes) dependent on external conditions. While the modification of the internal electric field is an important factor that drives the functioning of the device, presence of various interfaces/layers in the device can induce various traps or barriers that can be detrimental to the mobility of charge carriers through the device. Perovskites are also characterized by low defect formation energies, soft crystal lattice and weak bonds [16] [17]. Soft crystal lattice also implies presence of high density of point defects that can lead to ion migration and charge accumulation as well as recombination during device operation. This correlation between ion migration and interfacial degradation subsequently leads to crystal structure deformation and degradation of the overall device [18] [19] [20] [21] [22]. Ion migration in inorganic halide perovskites has been reported as early as 1983 by Fueki *et al*. [23]. Xiao *et al*. [24] were the first to report ion migration in organic-inorganic hybrid perovskites, specifically on $MAPbI_3$ (Methylammonium Lead Iodide) lateral devices, by optical microscope. They coupled PTIR (Photothermal Induced Resonance) microscopy, XRD (X-ray diffraction) and EDX (Energy dispersive X-ray) to provide a direct evidence of MA^+ and I^- migration [25] [26]. Another direct experimental evidence of halide ionic migration under bias has been provided by GD-OES (Glow Discharge Optical Emission Spectroscopy) [27]. Evidence of various anion and cation migration has been reported in several studies [28] [29] [30] [31] [32].

Ion migration has been observed by many groups [32], which was first reported as one possible origin of the anomalous current-voltage hysteresis in 2013 by Snaith *et al*. [33]. Ion migration is related primarily to the modification of band bending and internal

electric field, and formation/passivation of defects [34] [35]. The recent work done by Thiesbrummel *et al*. focused on the impact of ion-induced field on the stability of perovskite solar cells [36]. In this work, we have focused on the influence of electrical biasing as well as ageing due to strong forward/reverse bias and air exposition in $MAPbI_3$. Literature relating to electrical biasing has been known to indicate its influence on ion-transport and accumulation [37]. Under normal cell operation, i.e. biasing conditions the movement of ions affects the built-in potential thus impacting the device performance. A number of techniques, in addition to the ones mentioned above, are used to understand the electrical properties as well as the degradation mechanism of these materials. EIS is used to analyze time dependent electrical characteristics enabling the extraction of mobile ions and charge accumulation as the interfaces [38] [39] [40] [18]. Capacitance-frequency (C-f) measurements are used to correlate changes in capacitance with observed hysteresis in *J-V* characteristics [41]. Mott-Schottky (M-S) analysis is used to determine the built-in potential of the solar cells giving indications to degradation mechanisms [42] [43].

However, current techniques struggle to distinguish different ion species and different migration paths. There are a number of inconsistencies between simulations and experimental results reported that require advanced characterization techniques such as X-ray microscopy. We have recently reported the study of co-evaporated $MAPbI_3$ utilizing STXM [44] [45] [46] with the goal of evaluating the utility of STXM for these materials. Among various synthesis routes of PSC's, such as various solution processed films (single step deposition [47], two step deposition [48] [49], rapid deposition crystallization [50], Lewis base adduct method [51] etc.) along with thermal techniques, we have chosen co-evaporation because it offers a route to highly homogeneous and reproducible perovskite films [52]. STXM allows to report on the chemical homogeneity and on ion-migration in these co-evaporated samples.

In this paper we have extended the above study by performing correlative EIS and STXM to track the chemical changes as well as ion-migration in $MAPbI_3$ and films that were biased in-situ (in STXM) as well as ex-situ. We have also presented results from solar cells that were aged in air. Based on these results we propose a possible route of ion-migration in these films.

II. Experimental:

1- Structure and fabrication of the perovskite solar cells.

Figure 1(a) shows the schematic of a planar perovskite solar cell structure synthesized by co-evaporation and is investigated in this work. The analyzed PSCs were of an inverted planar structure in which PEDOT:PSS (Poly(3,4-ethylenedioxythiophene:polystyrene sulfonate) was used as hole transport layer (HTL) and C_{60} as electron transport layer (ETL). A thin layer of Bathocuproine (BCP) is used as hole blocking layer and silver is used as the cathode. All the layers were vacuum

deposited on top of a glass substrate. Figure 1(b) shows the SEM (Scanning Electron Microscopy) image of the cross section of a fabricated device displaying the different layers clearly. The active area of the device is 0.28 cm^2. Figure 1(c) also shows the energy band alignment of the solar cell.

The full fabrication process of the devices is described in Supporting Information (SI).

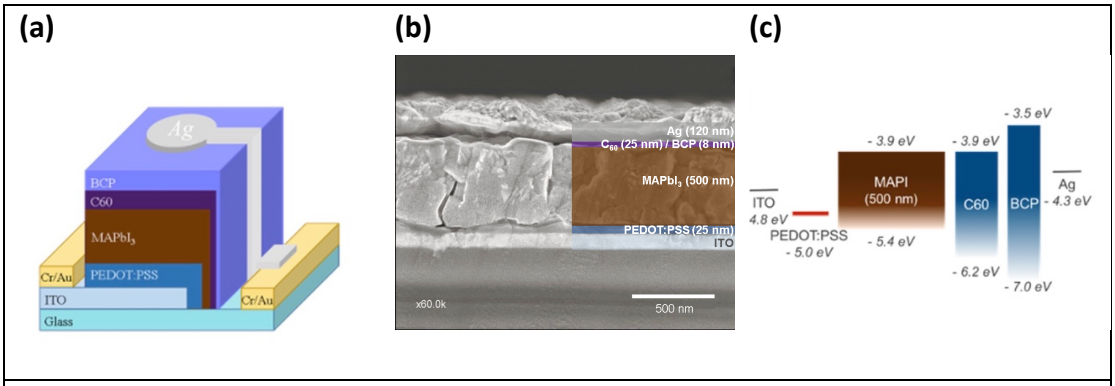

Figure 1 (a) Schematic of the structure of the perovskite solar cell analyzed in this study, (b) cross-sectional SEM image, (c) energy band diagram of the solar cell before contacting the different layers.

2- STXM measurements

STXM instrument: The experiments were conducted using a Research Instruments STXM, provided by Research Instruments (RI) GmbH, Germany, at the HERMES beamline [53] at the synchrotron SOLEIL facility. A Fresnel Zone Plate with a 25 nm outer zone radius was used to focus a monochromatic X-ray beam onto the sample (~30 nm spot size). The sample was attached to a stage capable of raster scanning. A Photomultiplier Tube (PMT) was used to detect the transmitted X-rays. Throughout all measurements, the microscope chamber was held under vacuum at a pressure of 10^{-4} mbar. A linearly polarized incident X-ray of energy in the range of carbon K-edge (270-310eV), nitrogen K-edge (390-415eV) and iodine M-edge (615-800eV) energy was used for investigation. The dwell time for the stack of images was kept at 3 ms to minimize X-ray exposure. The ex-situ biased samples were deposited on glass as detailed above and were sectioned using FIB (Focused Ion Beam) as detailed below.

FIB sectioning: STXM measurement of ex-situ biased samples were performed on FIB sections. A thin layer of carbon and layer of platinum (2µm x 2µm x 20µm) were deposited to avoid any charge effects and for protection respectively. The selected area is isolated using the energetic gallium ion beam. Once the area is isolated, the milling process begins using a high current ion beam, and then the ion beam current is reduced as the lamella becomes thin (down to 0.8–1 µm). The lamella is then removed from the substrate with a micro-manipulator and transferred to a TEM sample grid. A second milling process using very low ion beam currents, is performed to thin the lamella until its thickness is about 150–200 nm. The lamella obtained is then removed from the FIB and placed under a controlled atmosphere in a transfer coffer in order to avoid air

exposure during sample handling. These samples were then transferred in a sealed box to the STXM chamber for measurements.

3- EIS measurement

EIS measurement was carried out by applying a small alternating voltage signal (V_{AC}) across the sample and measuring the alternating current response (I_{AC}) to extract the total impedance (Z).

In this study, the frequency range was from 10^{-2} to 10^{6} Hz. The DC bias was fixed to 0 V and AC voltage to 50 mV respectively. EIS measurements were performed with an SP-200 equipment by Biologic. EC-Lab software from Bilogics© was used to fit the experimental data from the Nyquist plot. Figure S2 shows the two equivalent circuits used to fit the experimental data in the present study.

III. Results and discussion:

1- Reproducibility and electrical properties of the devices:

In order to analyze the electrical characteristics of the co-evaporated solar cells produced, *J-V* curves and external quantum efficiency (EQE) measurements were performed.

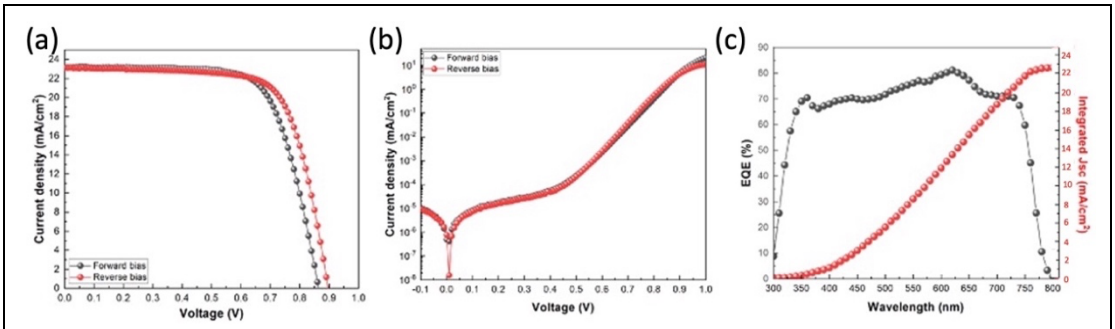

Figure 2: Current density-voltage curves of perovskite solar cells based on $MAPbI_3$ prepared by evaporation process measured (a) under 1-sun illumination and (b) under dark, (c) the corresponding EQE spectrum.

J-V characteristics of the perovskite solar cells under 1 sun is described in Figure 2(a), where we obtained a short circuit current density J_{SC} of 23.14 mA/cm^2, fill factor FF of 71.4 %, and an open circuit voltage V_{OC} of 0.90 V, leading to a power conversion efficiency PCE of 14.79 %. Hysteresis effect of the device was evaluated by measuring *J-V* curves in forward (from short-circuit to open-circuit voltage, denoted later as FB) and reverse scan direction (from open-circuit voltage to short-circuit denoted later as RB) at a scan rate of 10 mV/s. Hysteresis is typically presented by measuring *J-V* curves after prolonged pre-biasing at open-circuit voltage, large forward bias or reverse

bias when ions are accumulated at the interfaces. Hysteresis index (HI) was calculated using equation 1 and found to be a low value of 0.05.

$$HI = \frac{PCE_{RB} - PCE_{FB}}{PCE_{RB}} \qquad \textit{(Equation 1)}$$

Figure 2 (b) shows the dark *J-V* curve of the solar cells and it provides valuable information related with series resistance R_S, shunt resistance R_{SH} and FF (5.89 Ω, 1.26 kΩ, 68.5% for forward bias and 5.26 Ω, 2.56 kΩ and 69.5% for reverse bias). The dark current of the device under reverse bias is significantly low suggesting that the reference perovskite solar cell shows a low leakage current. In the forward bias region beyond 0.85 V, the injected current density is high indicating that the injection barrier between transport layer and perovskite is low.

The results show that device has a relatively high quality interfaces between perovskite layer and transport layers which results in a high FF. EQE spectrum of the reference device is plotted in Figure 2(c). A band gap of 1.53eV is obtained based on the EQE, which is comparable to the ideal value of 1.55eV for $MAPbI_3$ prepared by wet process.

In order to assess the stability of the reference perovskite solar cells, the device was stored in N_2 glove box and its *J-V* curves were measured periodically under 1 sun illumination by a solar simulator. Figure S3(a) presents the PCE and hysteresis index obtained from periodic measurement of *J-V* curve. The reference device maintained more than 90% of its initial efficiency after 8 weeks storage in N_2 with HI stable around 0.05 as well. The results verified that perovskite solar cells based on co-evaporated $MAPbI_3$ are more stable than those with solution-processed $MAPbI_{3-x}Cl_x$ and triple cations perovskite solution $(MA_{0.17}FA_{0.83})_{0.95}Cs_{0.05}Pb(I_{0.83}Br_{0.17})_3$ (3CP) fabricated in our laboratory. Solution-processed $MAPbI_{3-x}Cl_x$ and 3CP solar cells fabricated in LPICM maintained less than 60 % after 8 weeks storage in N_2. To check the reproducibility, a statistical histogram of PCE of 19 individual devices are shown in Figure S3(b). The average efficiency for the device is 12.51 % $\pm$ 2.28 %.

2- <u>Influence of ex-situ electric field:</u>

The EIS is measured for PSCs before and after applying different electric fields during *J-V* measurements. When the different layers of the solar cell are connected, an internal electric field (built-in field) is formed due to the difference in Fermi levels under equilibrium of HTL and ETL [54] [55] as can be seen in Figure S2. Figure 3 presents the EIS results of the PSCs before and after the measurements of the J-V curves.

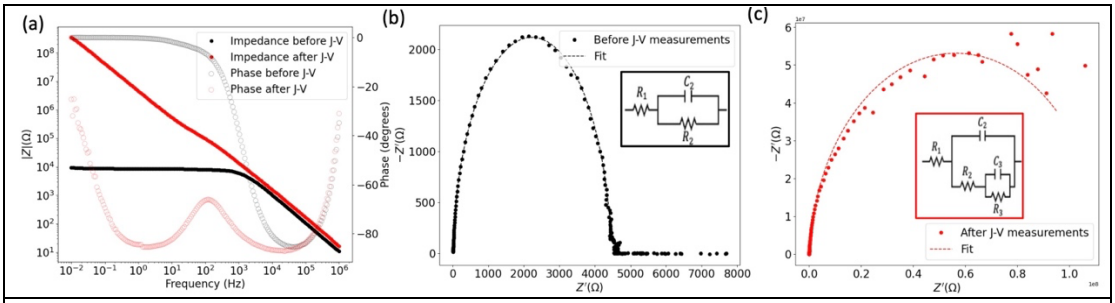

Figure 3(a): Bode impedance and phase plot of $MAPbI_3$ before and after applied electric field under dark conditions. (b) and (c) Measured Nyquist plots of $MAPbI_3$ reference solar cells before and after applying an electric field, respectively. The inset figures represent the corresponding equivalent circuits.

Before applying electrical bias, the complex impedance (|Z|) and its phase (Figure 3(a)) can be described by the equivalent circuit inset on Figure 3(b) . In the high-frequency region, the complex impedance (|Z|) curve has a slope of -1 with a phase close to -90 degrees which implies pure capacitance. On the other hand, in the low-frequency region, there is a plateau of the complex impedance (|Z|) with phase 0 degree, indicating a pure resistance. The geometric capacitance C_2 obtained by fitting the experimental data is 10.1 nF giving a relative dielectric constant of 20 closer to the value reported by other research groups using similar device architecture and thickness [56], [57], [58] [59].

After performing *J-V* measurements on the PSCs, the EIS technique is applied again. The total impedance (|Z|) at low-frequency region changes significantly with the reduction of the resistive plateau and the formation of a second capacitive behavior. Another phase of - 90 degrees at low frequency represents the building of a second capacitance. To analyze the impedance properties of the PSC in detail, the experimental data is fitted with equivalent circuit models. Figure 3(b) and (c) show the measured and fitted Nyquist plot of the reference PSC before and after applying an electric field, respectively. The equivalent circuits used in the fittings are shown in the inset of the Figure 3(b) and (c). The Nyquist plot of the PSC after biasing presents an additional RC element connected with R_2 in series in comparison with the equivalent circuit fitted for the fresh sample. The different circuit parameters, including R_1, R_2, C_2, R_3, and C_3 are extracted by fitting the Nyquist plot and are reported in Table 1.

Table 1: Characteristic parameters extracted by fitting the experimental data of Figure 3(b) and (c) with equivalent circuits.

Condition	R_1 (ohm)	R_2 (ohm)	C_2 (nF)	R_3 (ohm)	C_3 (nF)
Before *J-V* measurement	9.91	4.1×10^3	10.1	-	-
After *J-V* measurement	9.42	6.7×10^4	19.1	1.1×10^8	32

The resistance R_1 is most likely the contact resistance and was not significantly affected by the electrical biasing. R_1 is mainly linked to R_S which could be also estimated from *J-V* measurement preferably under dark conditions.

Moreover, after the *J-V* measurements, R_2 increased indicating that the charge carrier recombination is affected by the electrical field. As expected, the geometrical capacitance (C_2), related to the thickness of PSCs, was not affected by the electric bias. On the other hand, the capacitance (C_3) observed at low frequency can be considered as electrode polarization caused by interfacial phenomena, i.e., by ionic charge accumulation at the interfaces of $MAPbI_3$ [59], [60], [61], [62].

To study the effect of a strong electric field on the performance of PSCs, we conduct *J-V* measurements before and after applying a voltage of ±2.5 V for 15 minutes. Figure 4 illustrates the changes in *J-V* characteristics before and post-biasing and encloses the characteristics parameter of the photovoltaic performance of PSCs under each condition. The initial PCEs of the two fresh solar cells, denoted as device 1 and device 2, are 14.74% and 11.79%, respectively. For device 1, upon application of a positive bias of 2.5 V, a PCE of 11.02% with a J_{SC} of 22.55 mA/cm^2, a FF of 61.4%, and a V_{OC} of 0.80 V are obtained (Figure 4(a)). A noticeable decrease in J_{SC}, V_{OC}, and R_{SH} is observed, resulting in reduced FF and PCE. Particularly, the decline in R_{SH} and FF suggests the formation of defects at the interfaces induced by the pre-biasing. Furthermore, *J-V* hysteresis behavior with HI of 0.46 indicates that the electric bias induces strong modifications in PSCs electrical characteristics.

On the other hand, application of negative bias induces a diode breakdown. Thus, the changes in electric properties induced by the negative electric bias is significantly stronger than those induced by the positive bias despite having the same magnitude.

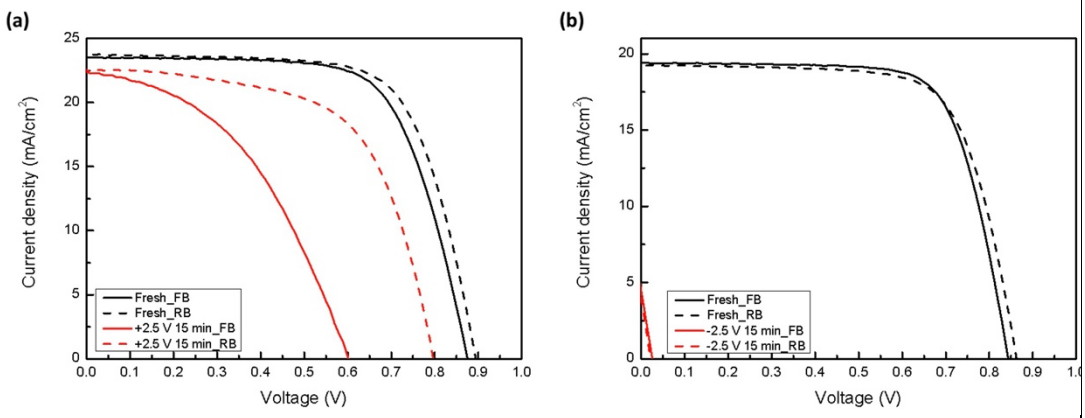

Figure 4: J-V characteristics of $MAPbI_3$ PSCs (a) before and after applying an electric field of +2.5 V for 15 minutes and (b) before and after applying an electric bias of -2.5 V for 15 minutes.

Table 2: Summary of photovoltaic parameters of $MAPbI_3$ PSCs with the fresh condition and after applying the electric bias of +2.5 V and -2.5 V during 15 minutes, (FB is forward scan and RB is reverse scan respectively).

Measurement conditions		Scan direction	V_{OC} (V)	J_{SC} (mA/cm^2)	FF (%)	R_S (ohm)	R_{SH} (ohm)	PCE (%)
Device 1	Fresh	FB	0.88	23.51	68.5	5.89	1260	14.09
		RB	0.89	23.74	69.4	5.26	2560	14.74
	+2.5 V	FB	0.60	22.39	43.8	10.7	273	5.9
		RB	0.80	22.55	61.4	5.58	861	11.02
Device 2	Fresh	FB	0.84	19.40	72.5	5.71	2890	11.86
		RB	0.86	19.27	70.9	5.69	2010	11.79
	-2.5 V	FB	0.03	4.57	25.0	5.75	5.71	0.03
		RB	0.03	4.10	22.1	5.20	5.46	0.02

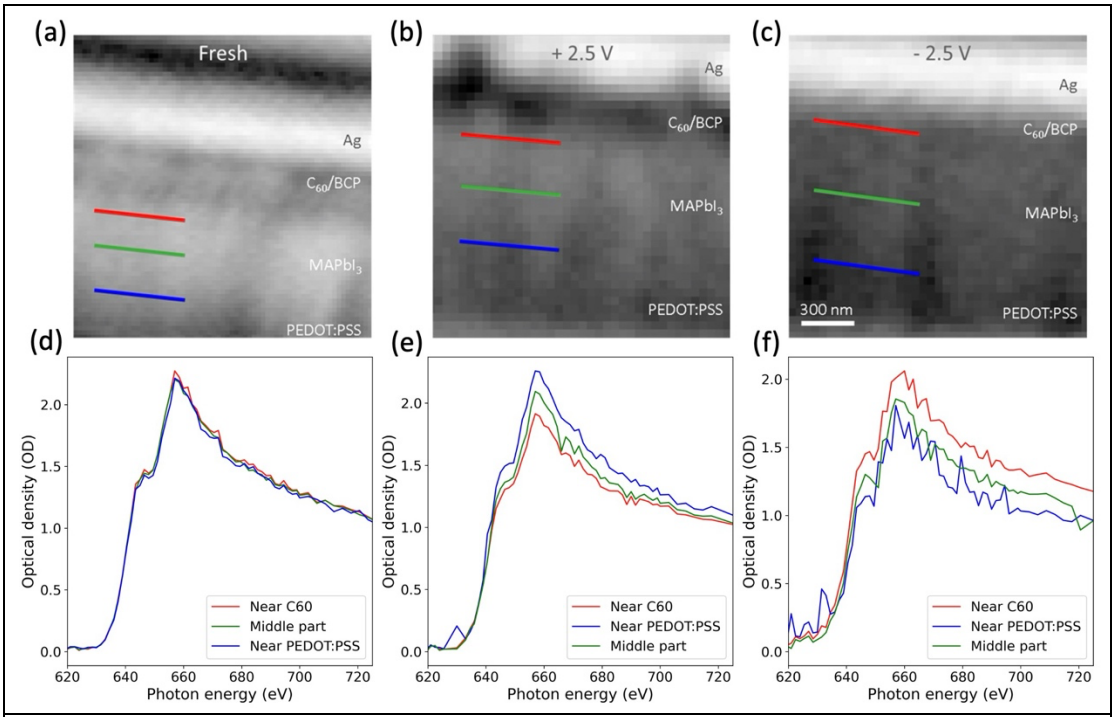

Figure 5: STXM images of FIB sections of (a) fresh $MAPbI_3$ PSCs and the PSCs after applying (b) +2.5 V and (c) -2.5 V for 15 minutes. The STXM images were measured at 616.5 eV. I M-edge NEXAFS spectra of (c) fresh $MAPbI_3$ layers between PEDOT:PSS and C_{60}, and the layer after applying (e) +2.5 V and (f) -2.5 V. The colors of the NEXAFS spectrum line in (d), (e), and (f) correspond to the regions marked in the same color in the corresponding image (a), (b) and (c).

Figure 5(a), (b), and (c) present STXM images (616.5 eV) of cross-sections of three $MAPbI_3$ PSCs (FIB sections), in which (a) is a fresh sample and (b) and (c) corresponds to a PSCs after applying an ex-situ electric field of +2.5 V and -2.5 V, respectively. Figure 5(d), (e), and (f) correspond to X-ray absorption spectra (XAS) at the I M-edge of the bulk of the $MAPbI_3$ layer and the region near PEDOT:PSS and C_{60} in each sample of Figure 5(a), (b), and (c), respectively.

In the fresh sample (Figure 5 (a) and (d)), the form and the intensity of the spectra in a whole region, including the middle part (green) and two interfaces between $MAPbI_3$ and charge transport layers (PEDOT:PSS (blue) and C_{60} (red)), are identical. This indicates a morphological and chemical homogeneity of the iodine content in the $MAPbI_3$ layer. Application of a positive bias of 2.5 V leads to a decrease in optical density (OD) from PEDOT:PSS layer to C_{60} (Figure 5(b) and (e)). This indicates that negative iodine ions migrate toward PEDOT:PSS under positive electric bias. On the contrary, the OD intensity of I decreases from C_{60} to PEDOT:PSS when a voltage of -2.5 V is applied (Figure 5(c) and (f)), re-emphasizing I^- ion migration under an electric field. Negative bias also introduces change of shape in the pre-edge region indicating chemical changes. Changes upon negative biasing are relatively stronger compared to positive bias. This is in accordance with what was observed through *J-V* measurements. In fact, under reverse bias, the electric field in the device is greater than under forward bias of the same magnitude. This is because the applied voltage adds to the built-in potential in reverse bias, while it subtracts from the built-in potential in forward bias. (see Figure S4 in the SI).

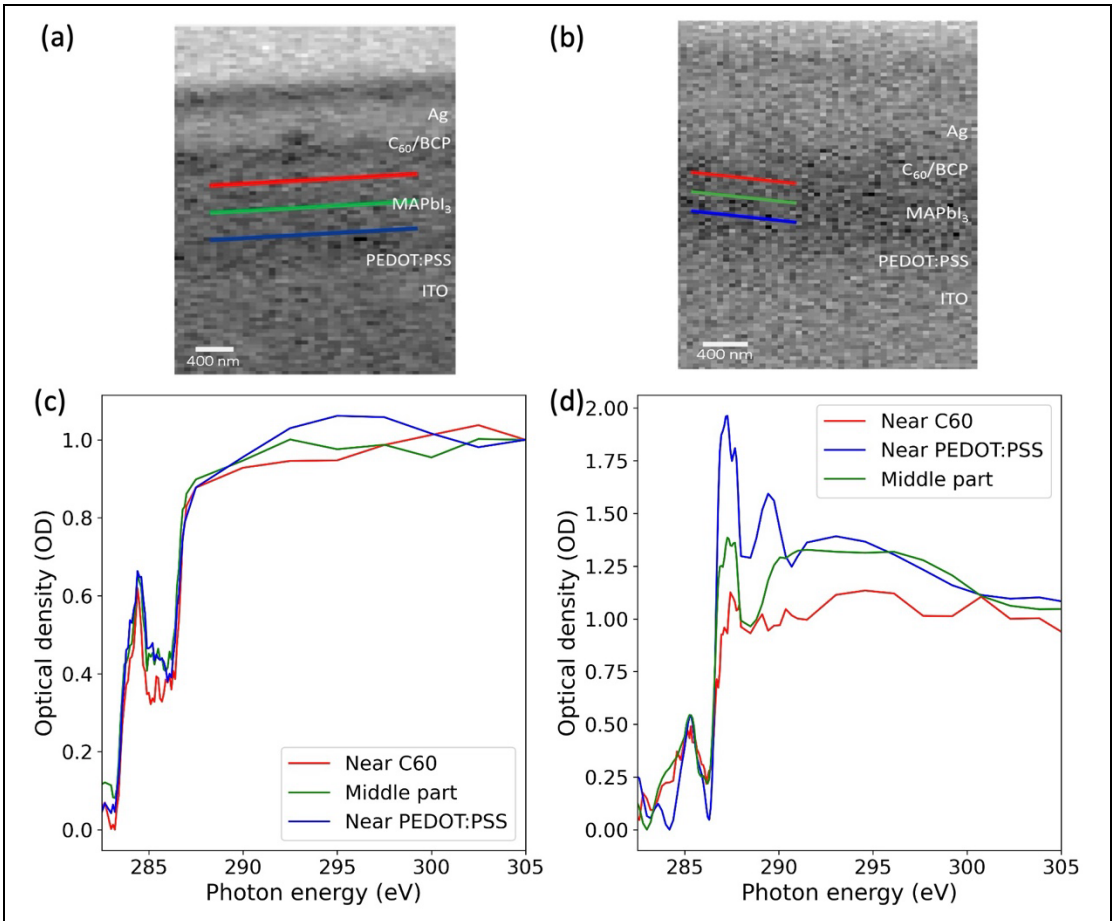

Figure 6: (a) Cross-section STXM images and (c) C K-edge NEXAFS spectra of fresh $MAPbI_3$ PSCs. (b) Cross-section STXM images and (d) C K-edge NEXAFS spectra of $MAPbI_3$ PSCs after applying -2.5 V for 15 minutes. The colors of the NEXAFS spectrum line in (c) and (d) correspond to the regions marked in the same color in the corresponding image (a) and (b).

In order to further understand the electric field-induced degradation of the $MAPbI_3$ layer in the device, XAS at the C K-edge of $MAPbI_3$ for the fresh sample and for the sample that was negatively biased was measured (limited beamtime did not allow the measurement of a positive bias sample). For the fresh sample, the various spectra are similar with only minor differences, underlining the homogeneity of the deposition (Figure 6(a) and (c)). The C1s→π* feature in Figure 6(c) is much more pronounced than in Figure 6(d), especially relative to the σ* region (high energy). This could be due to saturation of the signal above the absorption edge (>287 eV). For the negatively biased sample (Figure 6 (b) and (d)), the OD intensity of C K-edge at 291 eV decreases from PEDOT:PSS to C_{60}, which is the opposite direction of I^- migration under the electric biasing. Furthermore, the pre-edge spectral feature corresponding to C1s→π* (C=C) at 286 eV is higher, and the one corresponding to C1s→σ* (C-H) at 289.5 eV is lower at the interfaces than those of the central region of $MAPbI_3$. This implies that C-H bonds in methylammonium are most likely broken upon the application of electrical bias. This is followed by the formation of new bonds at the interface. While we have carefully chosen the region to avoid an overlap with the interfaces, we cannot discount the possibility of the unsaturated bonds arising from the PEDOT:PSS, C60 or BCP. We note

in addition, the OD corresponding to C1s→π* (C=O) at ~287.5 eV is much stronger at the interface between $MAPbI_3$ and PEDOT:PSS. This clearly points to the possibility of the formation of new chemical bonds and perhaps the fragmentation of the original ones. Hence we observe not only the migration of I^- and MA^+ ions but we also observe the changes in the resonance of iodine and the chemical bonds in MA^+ at the interfaces between $MAPbI_3$ and HTL/ETL using STXM.

3- STXM results - Before and after in-situ electrical biasing

Figure 7 shows the image and schematics of the in-situ electrical biasing system used for the analyzed PSC that were measured in STXM. Image of the biasing system mounted inside the STXM chamber. Further Figure 8(a) and (b) shows the STXM images taken at 662 eV (above the I M-edge) before and after applying electrical bias.

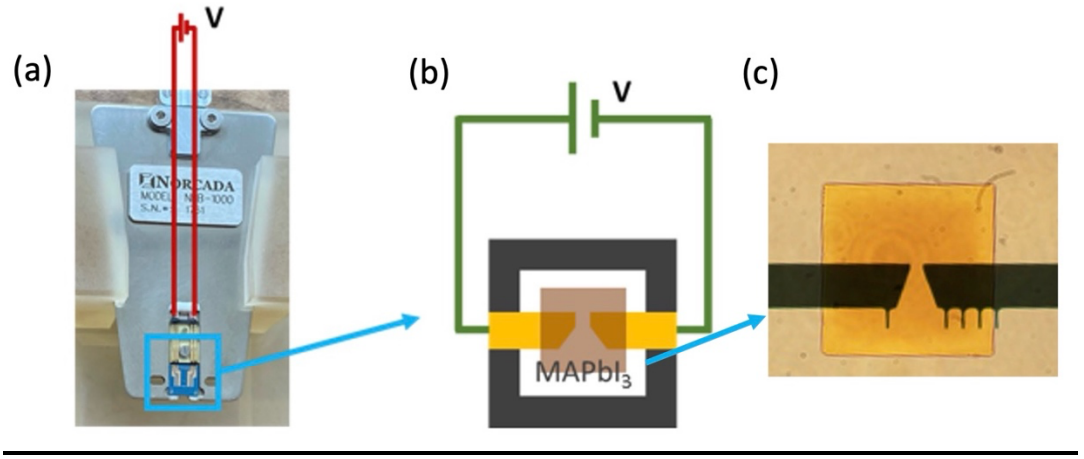

Figure 7: (a) Electric biasing system including electric biasing chip, its holder, electric biasing controller (b) Close-up of electric biasing chip and holder. (c) Light microscope image of $MAPbI_3$ film on the electric biasing chip.

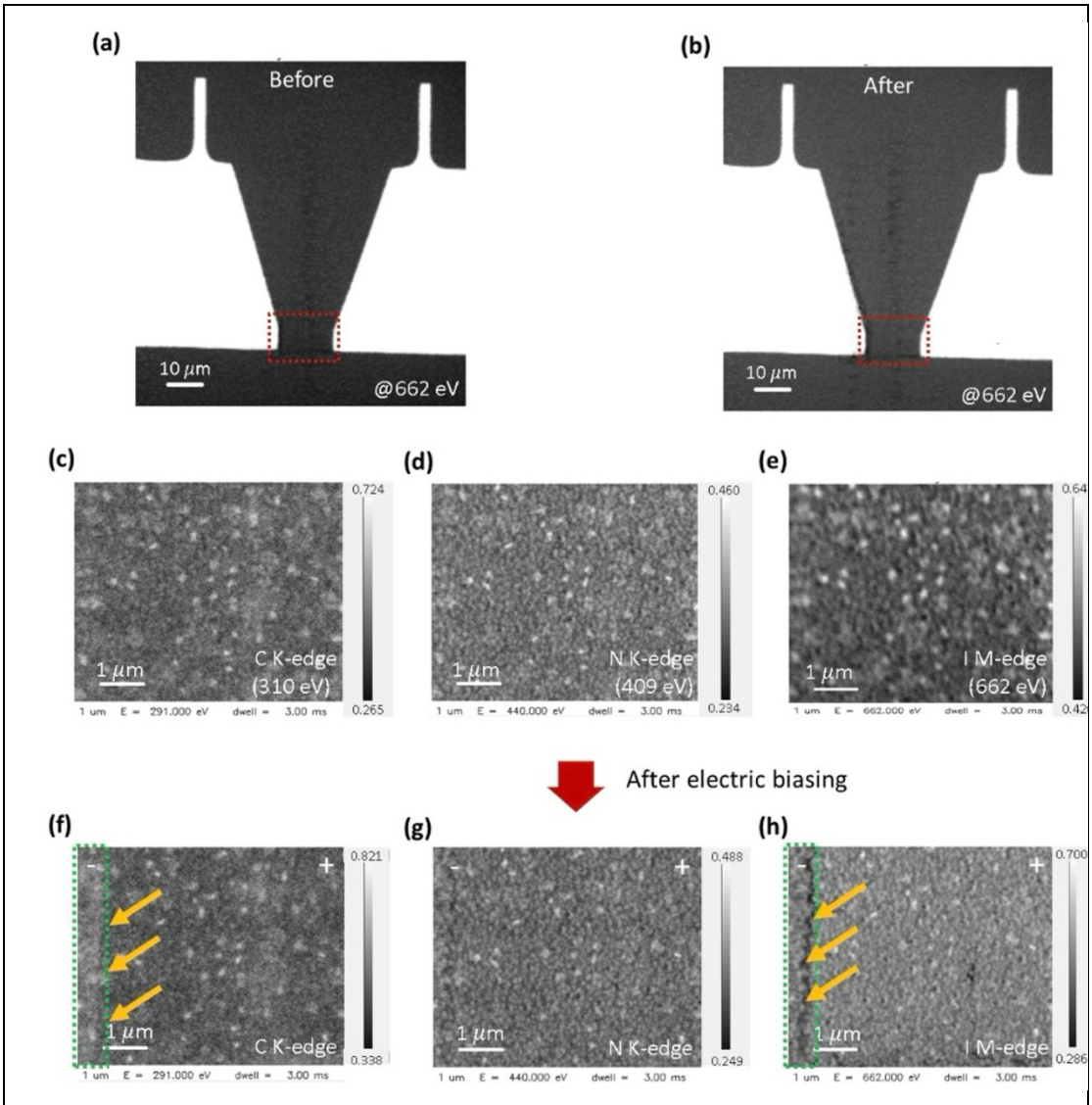

Figure 8: STXM images at 662 eV of $MAPbI_3$ (a) before and (b) after applying a positive electric field. Red dotted regions in (a) and (b) indicate the region of $MAPbI_3$ between two Au electrodes with the shortest distance. Zoomed-in STXM images of the red dotted region before biasing at (c) 310 eV (C K-edge), (d) 409 eV (N K-edge), and (e) 662 eV (I M-edge). Zoomed-in STXM images of the red dotted region after biasing at (f) 310 eV (C K-edge), (g) 409 eV (N K-edge), and (h) 662 eV (I M-edge).

The red dotted square region in Figure 8(a) and (b) was chosen as the region of interest and investigated closely. Figure 8(c), (d), and (e) indicate STXM images taken before biasing at C K- edge, N K-edge, and I M-edge, respectively. These three images clearly imply that carbon, nitrogen, and iodine are homogeneously distributed before biasing. Upon the application of the electric field significant changes can be observed near the cathode. In Figure 8(f), the OD of carbon near the cathode (green dotted region) is relatively higher than in other regions. On the other hand, the OD of iodine (Figure 8(h)) near the cathode shows a strong dip. Negative ions of iodine have migrated to the anode under a positive electric field, as has also been observed in other studies [56] [63], [64].

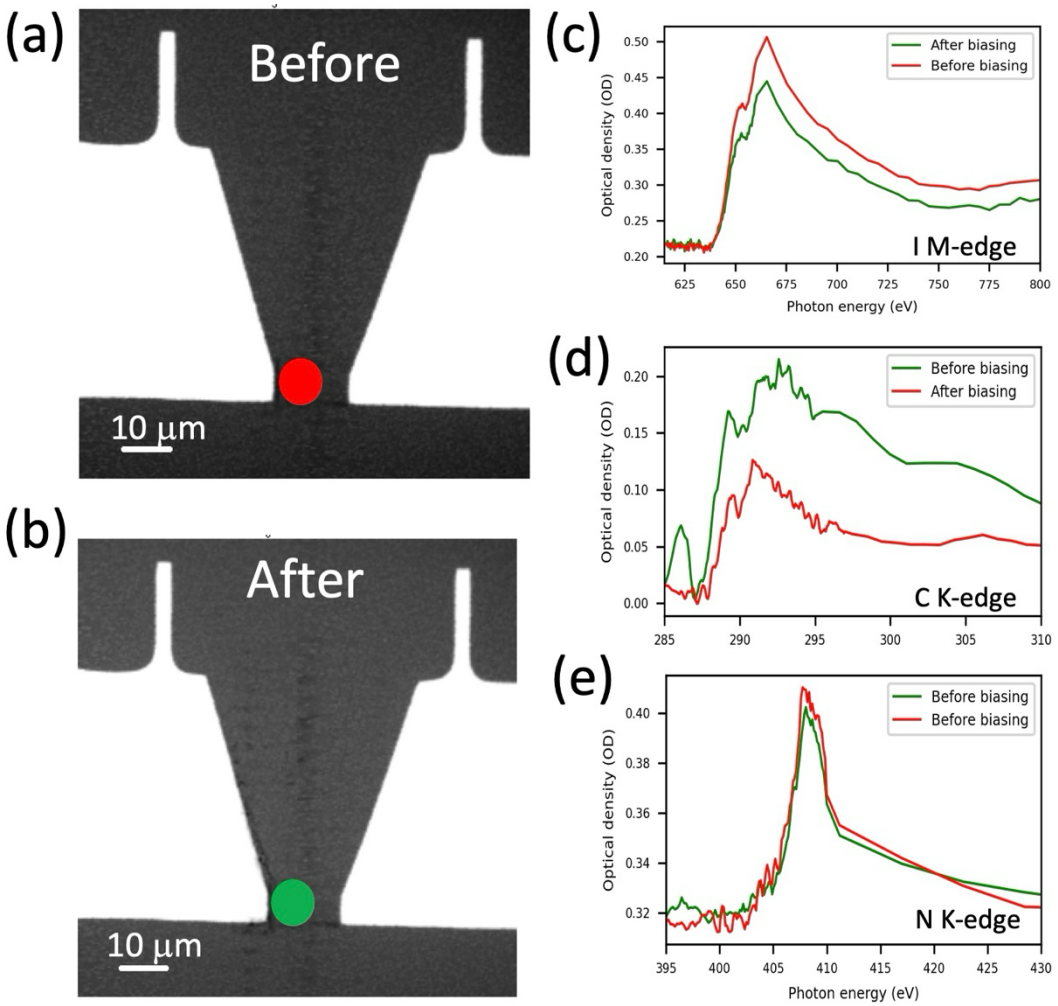

Figure 9: STXM OD images at 662 eV of $MAPbI_3$ (a) before and (b) after applying a positive electric bias. The region of interest near the cathode has been marked in red and green in (a) and (b). I M-edge (c) C K-edge, and (d) N K-edge NEXAFS spectra of MAPbI3 before and after electric biasing as extracted from the ROI.

It is interesting to note that only a small change was observed in nitrogen OD Figure 8(g)) under electric bias, although the OD of carbon near the cathode increases relatively significantly. To analyze the change of MA^+ under electric bias in detail, the spectra that cover the I M-edge (Figure 9(c)), C K-edge (Figure 9 (d)), and N K-edge (Figure 9 (e)) are extracted from the region of $MAPbI_3$ near the cathode (Figure 9 (a) and (b)). In the three spectra, the red lines indicate the XAS spectra before applying an electric field, while the green lines indicate the XAS spectra after applying the electric field.

In Figure 9(c), the OD intensity of I M-edge at 662 eV significantly decreases after applying an electric field, which indicates that the iodine ions near the cathode migrate in the direction of the anode, coherent with ex-situ biasing results. In the case of carbon, there is a change in the opposite direction implying that there is indeed a migration of

carbon atoms towards the cathode as well (Figure 9(d)). The spectra show additional changes in the C K pre-edge. The minor peak related to C1s→σ* (C-H) at 289.5 eV slightly increases. In addition, the pre-edge spectral features of C1s→π* (C=C), which are negligible before applying electric bias, appear after applying the electric field. On the other hand, minor peak of C1s→π* (C=O) disappears or is enveloped by other high energy broader features after electrical bias. With the changes in peaks in the C K pre-edge region, we can guess that the electric field results in the change of chemical bonds associate with MA+. This increase in carbon content is perhaps accompanied by an increase the nitrogen content as well, indicated by the overall edge jump (440 eV) for the spectrum of the biased sample as compared to the unbiased sample.

For clarity, below is the point-wise summary of observations:

- Iodine is observed to migrate away from the cathode. Spectral data also indicate that the average iodine content decreases near the cathode. OD images at 662 eV show a systematic decrease in the OD near the cathode.
- Spectral data and OD image at 291 eV indicate a clear increase in the carbon content near the cathode. This increase is an overall increase in the carbon content, i.e., not a particular bond-specific species, and can be ascertained from the difference between the 291 eV and 285 eV images.
- While there is an increase in carbon content, a similar increase is not clearly observed in the nitrogen content in Figure 8(g) but is seen in Figure 9. This indicates a decomposition of the MA^+ ions under an electric field.

4- Proposed mechanism of electric field-induced degradation in $MAPbI_3$

A mechanism of electric field-induced degradation in $MAPbI_3$ is proposed to describe the origin of the defect at the interface. Herein, the chemical changes related to the observed phenomena in the PSCs are explained by considering the dynamics in three physically distinct regions across the $MAPbI_3$ layer: the bulk of $MAPbI_3$ layer, and the region close to the interfaces between the $MAPbI_3$ and C_{60} and PEDOT:PSS layer (Figure 10). In the $MAPbI_3$ layer, mobile iodine ions (I^-) and iodine vacancies (V_I^+) are formed upon an electric bias. The negative iodine ions migrate toward the C_{60} layer under the electric field. In the case of MA^+, two decomposition pathways can be considered. One pathway could lead to the formation of CH_3NH_2 with HI, which is formed with H from MA^+ and mobile I^-. The other pathway leads to NH_3 and CH_3^+. The positive ion CH_3^+ can react with I^- forming CH_3I, or it can migrate into PEDOT:PSS. In the case of nitrogen, CH_3NH_2 and NH_3 are neutral and do not migrate significantly under an electric field, which is evident from the relatively homogeneous XAS spectra of N in all regions (Figure 9).

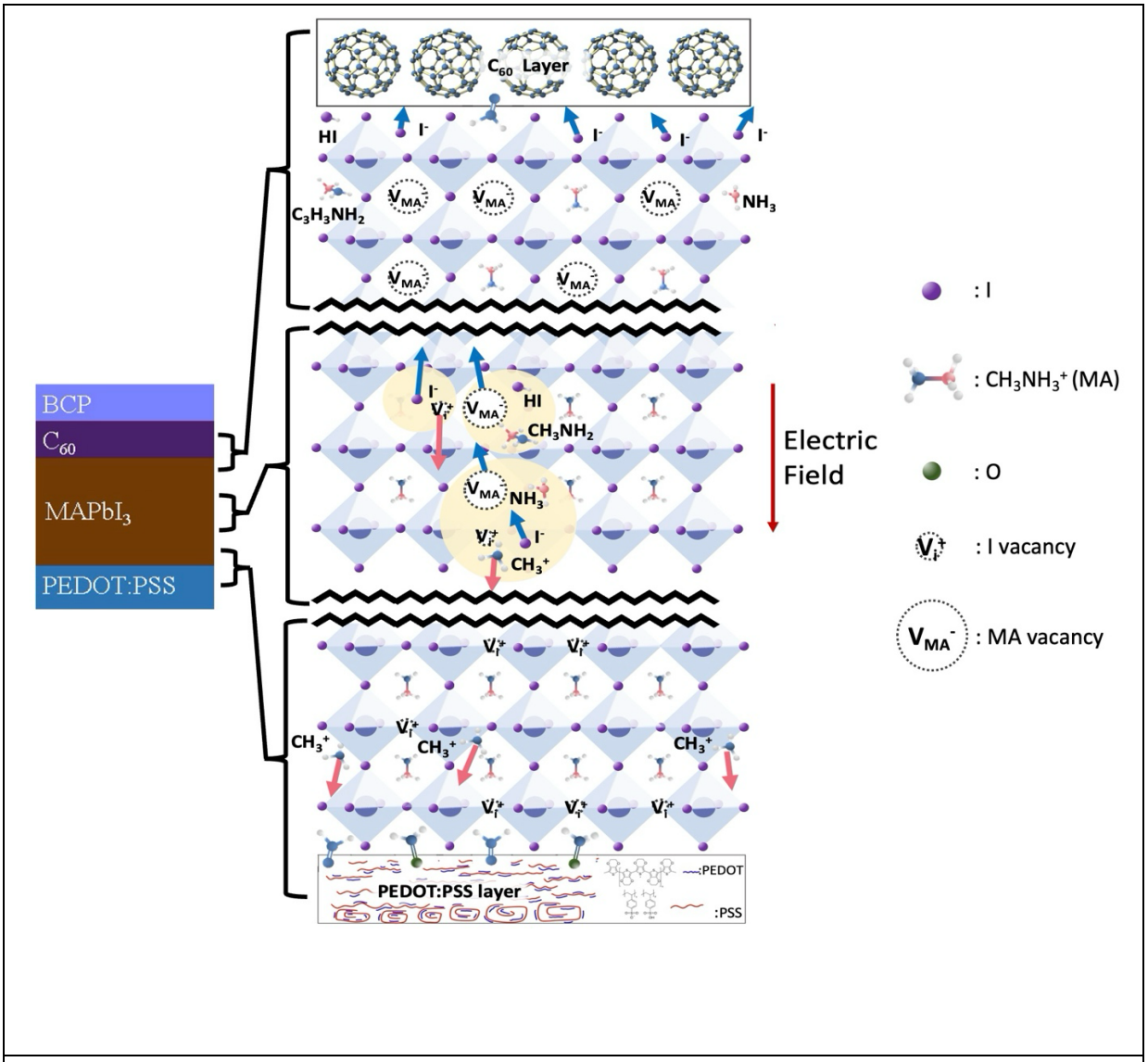

Figure 10: Schematic of the proposed degradation process in $MAPbI_3$ upon negative electrical bias

In $MAPbI_3$ near C_{60}, the same chemical reaction of iodine and organic cation induced by an electric field occurs. In addition, the mobile iodine ions and methylammonium vacancies (MA^+) accumulate at the interface between $MAPbI_3$ and C_{60}. The ions and vacancies lead to the formation of R_3 and C_3 and J-V hysteresis in J-V curves. Furthermore, some CH_3^+ ions can react with the adjacent C_{60}/BCP layer, leading to the formation of species of the type $H_2C{=}M$ (M is an atom or a molecule originating from C_{60} and BCP. These contribute to an increase in the peak intensity of feature C1s→π* (C=C) at 286 eV and decrease in the intensity of feature C1s→σ* (C-H) at 289.5 eV in XAS spectra Figure 6(b). The formation including the C=C double bond at the interface acts as a defect leading to an increase in R_3 of EIS results and a decrease in R_{SH} measured by J-V characteristics.

Lastly, in the $MAPbI_3$ layer near PEDOT:PSS, the formation of mobile iodine and the decomposition of organic cation continues as well. Upon negative bias, the positive ions of CH_3^+ and V_I^+ are accumulated at the interface, which contributes to R_3 and C_3

in EIS results. At the interface between $MAPbI_3$ and PEDOT:PSS, we hypothesize the breakdown of C-N bond and the formation of C=C as a result of reaction of CH_3^+ ions with the PEDOT:PSS. Furthermore, the use of methanol treatment during the deposition of PEDOT:PSS results in phase separation of these two components enabling the increase in conductivity of this layer. The oxygen ion in PSS, resulting from the phase separation, reacts with CH_3^+. This would lead to the formation of C=O bond subsequently increasing peak intensity of C1s→π* (C=O) transition at 287.5 eV. In addition, the diffusion of oxygen from ITO could also react with CH_3^+ forming C=O. The products formed by the reactions at the interface act as defects which affects the electrical properties in PSCs.

Through this correlation between the results electrical characterization including EIS and *J-V* curves and STXM results, we can propose a reliable hypotheses of electric field-induced degradation in PSCs. During the degradation process, ion migration and the formation of defects at the interface occurs. They affect the electrical characteristics including deterioration of photovoltaic performance and appearance of another impedance parameter which is found in the *J-V* curves and EIS results. Through the STXM results, we can identify the mobile iodine as well as CH_3^+ ions. In addition, the formation of defects at the interface can be explained based on changes in the chemical bonds of organic components at the interface in the STXM spectra.

Using the reference solar cell, we have studied the change in the $MAPbI_3$ bulk and the interfaces between $MAPbI_3$ and charge transport layers caused by an electric field from an electrical and chemical point of view. Firstly, the influence of the electric field on the impedance of PSCs was investigated using EIS. After applying an electric field, R_2 resistance determined by nonradiative charge recombination increases, and a second capacitance (C_3) at a low frequency is observed. The second capacitance is interpreted as a charge accumulation layer at interfaces. These results are coherent with the *J-V* curves of $MAPbI_3$ solar cells after applying an electric field that the shunt resistance decreases, and the hysteresis index increases. Additionally, the evolution of the reference solar cells under exposure to air was studied with *J-V* curves and impedance spectroscopy.

5- Ageing in air:

Figure 11(a) (b) and (c) show J-V curves measured under RB and FB scans taken at different stages of ageing of $MAPbI_3$, at 0 days, 14 days and 31 days, respectively while stored in dark conditions. While there are only minor changes for the forward scan, the FF of the *J-V* curve with RB direction decreases gradually with time. Interestingly, the hysteresis is inverted and HI (see equation 1) increases to negative values indicating device degradation. This result implies that the amount of accumulated mobile I^- ions and/or bulk/interface recombination rate increases upon ageing in air Figure 11(d).

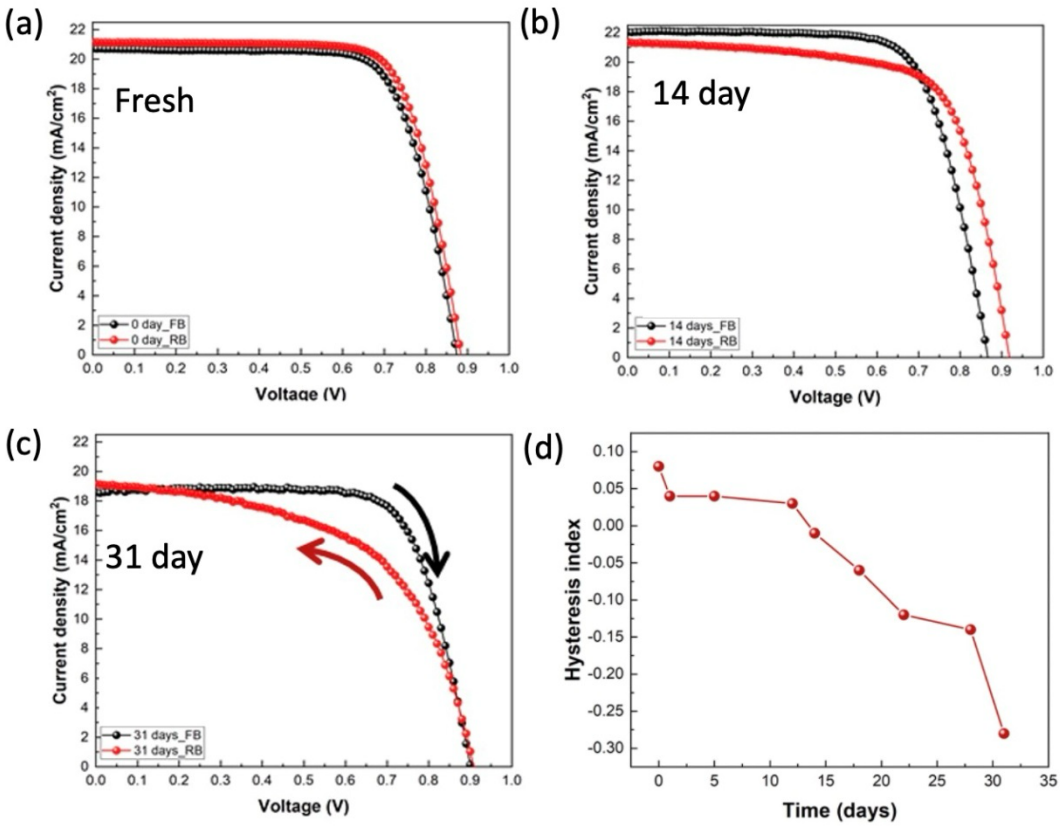

Figure 11: Current density-voltage (J-V) curves of $MAPbI_3$ as a function of ageing (a) fresh, (b) 14 days & (c) 31 days. (d) Evolution of hysteresis index.

Figure 12 shows impedance data collected from fresh and aged samples at various ageing intervals. In Bode plots (Figure 12 (a) and (b)), the fresh sample shows a pure capacitance with a phase angle close to -90 degrees at high frequency (10^4-10^5 Hz) and a resistive plateau at low frequency.

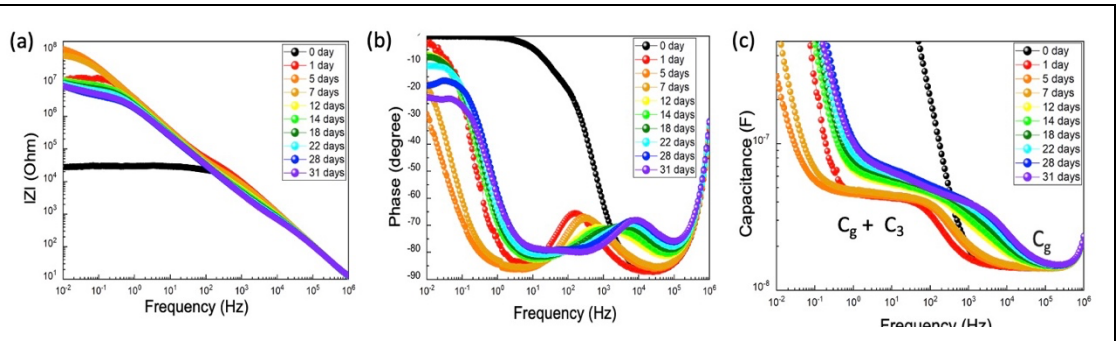

Figure 12: EIS characteristics evolution as a function of ageing time for optimized $MAPbI_3$ solar cell. (a) Complex impedance versus frequency. (b) Phase versus frequency. (c) Capacitance versus frequency.

In the Bode impedance plot (Figure 12(a)), the complex impedance (|Z|) shows a progressive change of the resistive behavior at low and intermediate frequency range with time, while no modification is observed at high frequency. At intermediate

frequency (10^2-10^3 Hz), |Z| decreases gradually upon ageing. In the Bode phase plot (Figure 12 (b) there is a phase close to -90 degrees at 100 kHz in the fresh sample. Upon ageing for five days, a second capacitive behavior emerges by the phase close to -90 degrees at a lower frequency range (1 Hz - 10 Hz). This feature at 1 Hz - 10 Hz is attributed to the charge accumulation layers occurring at the interfaces between MAPbI3 and selective contact layers. After 5 days, the total impedance (|Z|) and the magnitude of the phase decrease gradually from -90 to -80 degrees over time, indicating the loss of the pure capacitive property in the aged PSCs.

In Figure 12(c), only a single capacitance ($C_2 = C_g \sim 14$ nF, derived from fitting impedance data) is obtained at the high-frequency corresponding to the geometrical capacitance (Cg). In the high-frequency region, the conductivity of halide perovskite is too low for the photovoltaic system to respond fast enough to the high-frequency AC excitation, which has the system behave like an insulator. Therefore, the geometrical capacitance is defined as:

$$C_g = \varepsilon_0 \times \varepsilon_r \times \frac{A}{t} \qquad \textit{(Equation 2)}$$

where ε_0 is the dielectric constant of vacuum (8.8541×10^{-12} F/m), ε_r is the relative dielectric constant, A is the area, and t is the thickness of the absorber layer.

For the interpretation of the experimental data, we can use the electrical circuit in Figure S2(b) and Figure S6 (g). The fresh sample shows mostly two RC components (Figure S2(b)). R_2C_2 is related with the bulk and the geometrical capacitance and R_3C_3 could be related to the capacitance in one of the interfaces of the perovskite/transport layer and is promoted by the presence of one of the ions. During the aging, another RC elements appears (R_4C_4). One hypothesis is that R_4C_4 could be related to a second ion migration different to the one associated to R_3C_3 [65]. As both, R_3C_3 and R_4C_4 evolve with time an increase of the mobile ion concentration and ion mobility is expected. The second option is the creation of an interface barrier which hinders the flow of the current promoting an inversion of the hysteresis observed on the *JV* measurements [66]. It is worthy to note that *J-V* hysteresis increases with ageing time resulting from charge accumulation at the interface of PSCs device.

IV. Conclusion :

In this study we have evidenced the mechanisms of organic-inorganic perovskite solar cells degradation when exposed to air and under electrical stress. Firstly, we observed that the hysteresis index rises and the fill factor gradually decreases as $MAPbI_3$ solar cells age in air, signifying the buildup of mobile iodide ions over time.

EIS results indicate that the formation of charge accumulation layers at the interfaces is responsible for the emergence of a second capacitance (C_3) as a result of air ageing and biasing.

In-situ STXM measurements conducted under electrical bias show that negative bias causes the methylammonium (MA^+) cation to break down and cause iodide ions to migrate towards the cathode, which results in the formation of defects at the interfaces between the charge transport layers and the perovskite layer. These defects worsen the performance of the solar cell when it is electrically biased.

We have shown that the complementary use of EIS and STXM as characterization tools allows a thorough comprehension of the deterioration mechanisms in perovskite solar cells, emphasizing the important role of ion migration and interface reactions in achieving device stability and longevity.

V. Acknowledgement

The authors would like to thank Ecole Doctorale of École Polytechnique and Synchrotron SOLEIL for their Ph.D. grants assigned to Haeyeon Jun. Philip Schulz thanks the French Agence Nationale de la Recherche for funding under the contract number ANR-17-MPGA-0012. The authors would also like to thank Synchrotron SOLEIL for providing beamtime at HERMES beamline.

VI. References

[1] N. R. E. Laboratory. [Online]. Available: https://www.nrel.gov/pv/cell-efficiency.html.

[2] O. Almora, I. C. Cabrera, E.-E. Sule, F. Karen, K. Fukuda, F. Guo, J. Hauch, A. W. Y. Ho-Baillie, J. T. Jacobsson, R. A. J. Janssen, T. Kirchartz, M. A. Loi, X. Mathew, D. B. Mitzi and Nazeeruddin, "Device Performance of Emerging Photovoltaic Materials," *Advanced Energy Materials,* vol. 14, p. 2303173, 2024.

[3] C. C. Boyd, R. Cheacharoen and T. Leijtens , "Understanding Degradation Mechanisms and Improving Stability of Perovskite Photovoltaics," *Chemical Reviews,* vol. 119, no. 5, pp. 3418-3451, 2019.

[4] N. Aristidou, C. Eames, I. Sanchez-Molina, X. Bu, J. Kosco, M. S. Islam and S. A. Haque, "Fast Oxygen Diffusion and Iodide Defects Mediate Oxygen-Induced Degradation of Perovskite Solar Cells," *Nature Communications,* vol. 8, p. 15218, 2017.

[5] A. J. Pearson, E. G. Eperon, P. E. Hopkinson, S. N. Habisreutinger, J. T.-W. Wang, H. J. Snaith and N. C. Greenham, "Oxygen Degradation in Mesoporous Al2O3/CH3NH3PbI3-XClx Perovskite Solar Cells: Kinetics and Mechanisms.," *Advanced Energy Materials,* vol. 6, p. 1600014, 2016.

[6] N. Aristidou, I. Sanchez-Molina, T. Chotchuangchutchaval, and M. Brown, "The Role of Oxygen in the Degradation of Methylammonium Lead Trihalide Perovskite Photoactive Layers," *Angew. Chem. Int. Ed.,* vol. 54, 2015.

[7] A. Senocrate, T. Acartürk, G. Y. Kim, R. Merkle, U. Starke, M. Grätzel and J. Maier, "Interaction of oxygen with halide perovskites," *J. Mater. Chem. A,* vol. 6, pp. 10847-10855, 2018.

[8] Q. Jiang, J. Tong, R. A. Scheidt, X. Wang, A. E. Louks, Y. Xian, R. Tirawat, A. F. Palmstrom, M. P. Hautzinger, S. P. Harvey, S. Johnston, L. T. Schelhas, B. W. Larson, E. L. Warren, M. C. Beard, J. J. Berry, Y. Yan and K. Zhu, "Compositional texture engineering for highly stablewide-bandgap perovskite solar cells," *Science,* vol. 378, p. 1295–1300, 2022.

[9] H. Bencherif , F. Meddour, M. H. Elshorbagy, M. K. Hossain, A. Cuadrado, M. A. Abdi, T. Bendib, S. Kouda and J. Alda, "Performance enhancement of (FAPbI3)1-x(MAPbBr3)x perovskite solar cell with an optimized design," *Micro and Nanostructures,* vol. 171, p. 207403, 2022.

[10] S. M. Masawa, R. Bakari, J. Xu and J. Yao, "Progress and challenges in the fabrication of lead-free all-inorganic perovskites solar cells using solvent and compositional engineering Techniques-A review," *Journal of Solid State Chemistry,* vol. 317, p. 123608, 2023.

[11] S. Wang, H. Guo and Y. Wu, "Advantages and challenges of self-assembled monolayer as a hole-selective contact for perovskite solar cells," *Materials Futures,* vol. 2, p. 012105, 2023.

[12] Y. Yamada, M. Endo, A. Wakamiya and Y. Kanemitsu, "Spontaneous defect anni- hilation in CH3NH3PbI3 thin films at room temperature revealed by time- resolved photoluminescence spectroscopy," *J. Phys. Chem. Lett.,* vol. 6, no. 3, pp. 482-486, 2015.

[13] C. Fei and H. Wang, "Age-induced recrystallization in perovskite solar cells," *Org. Electron.,* vol. 68, pp. 143-150, 2019.

[14] S. Shin and H. Shin, "Aging of perovskite solar cells: a mini review," *Materials Today Energy,* vol. 37, p. 101381, 2023.

[15] S. Bae, S. Kim, S. -W. Lee, K. J. Cho, S. Park, S. Lee, Y. Kang, H. -S. Lee and D. Kim, "Electric-Field-Induced Degradation of Methylammonium Lead Iodide Perovskite Solar Cells," *J. Phys. Chem. Lett.,* vol. 7, pp. 3091-3096, 2016.

[16] J. M. Frost and A. Walsh, "What is Moving in Hybrid Halide Perovskite Solar Cells?," *Acc. Chem. Res.,* vol. 49, pp. 528-535, 2016.

[17] M. Saliba, J. -P. Correa-Baena, M. Grätzel, A. Hagfeldt and A. Abate, "Perovskite Solar Cells: From the Atomic Level to Film Quality and Device Performance," *Angew. Chem. Int. Ed.,,* vol. 57, pp. 2554-2569, 2018.

[18] S. Kim, S. Bae, S. -W. Lee, K. Cho, K. D. Lee, H. Kim, S. Park, G. Kwon, S. -W. Ahn, H. -S. Lee and D. Kim, "Relationship between ion migration and interfacial degradation of CH3NH3PbI3 perovskite solar cells under thermal conditions," *Sci. Rep.,* vol. 7, p. 1200, 2017.

[19] P. Roy, N. K. Sinha, S. Tiwari and A. Khare, "A review on perovskite solar cells: Evolution of architecture, fabrication techniques, commercialization issues and status," *Solar Energy,* vol. 198, pp. 665-688.

[20] C. Besleaga, L. E. Abramiuc, V. Stancu, A. G. Tomulescu, M. Sima, L. Trinca, N. Plugaru, L. Pintilie, G. A. Nemnes, M. Iliescu, H. G. Svavarsson, A. Manolescu and I. Pintilie, "Iodine Migration and Degradation of Perovskite Solar Cells Enhanced by Metallic Electrodes," *J. Phys. Chem. Lett.,* vol. 7, no. 24, p. 5168–5175, 2016.

[21] Y. Wang, T. Wu, J. Barbaud, W. Kong, D. Cui, H. Chen, X. Yang and L. Han, "Stabilizing heterostructures of soft perovskite semiconductors," *Science,* vol. 365, pp. 687-691, 2019.

[22] X. Ren, L. Zhang, Y. Yuan and L. Ding, "Ion migration in perovskite solar cells," *Journal of Semiconductors,* vol. 42, p. 010201, 2021.

[23] J. Mizukasi, K. Arai and K. Fueki, "Ionic conduction of the perovskite-type halides," *Solid State Ionics,* vol. 11, no. 3, pp. 203-211, 1983.

[24] Z. Xiao, Y. Yuan, Y. Shao, Q. Wang, Q. Dong, C. Bi, P. Sharma, A. Gruverman and J. Huang, "Giant switchable photovoltaic effect in organometal trihalide perovskite devices," *Nature Materials,* vol. 14, pp. 193-198, 2015.

[25] Y. Yuan, J. Chae, Y. Shao, Q. Wang, Z. Xiao, A. Centrone and J. Huang, "Photovoltaic Switching Mechanism in Lateral Structure Hybrid Perovskite Solar Cells," *Advanced Energy Materials,* vol. 5, no. 15, p. 1500615, 2015.

[26] Y. Yuan, Q. Wang, Y. Shao, H. Lu, T. Li, A. Gruverman and J. Huang, "Electric-Field-Driven Reversible Conversion Between Methylammonium Lead Triiodide Perovskites and Lead Iodide at Elevated Temperatures," *Advanced Energy Materials,* vol. 6, no. 2, p. 1501803, 2016.

[27] H. Lee, S. Gaiaschi, P. Chapon, A. Marronnier, H. Lee, J. -C. Vanel, D. Tondelier, J. -E. Bourée, Y. Bonnassieux and B. Geffroy, "Direct Experimental Evidence of Halide Ionic Migration under Bias in CH3H3PbI3-xClx-Based Perovskite Solar Cells using GD-OES Analysis," *ACS Energy Lett.,* vol. 2, pp. 943-949, 2017.

[28] J. Kim, S. -H. Lee and J. H. Lee, "The Role of Intrinsic Defects in Methylammonium Lead Iodide Perovskite," *J. Phys. Chem. Lett.,* vol. 5, p. 1312−1317, 2014.

[29] W. -J. Win, T. Shi and Y. Yan, "Unusual Defect Physics in CH3NH3PbI3 Perovskite Solar Cell Absorber," *Appl. Phys. Lett.,* vol. 104, p. 063903, 2014.

[30] K. X. Steirer, P. Schulz, G. Teeter, V. Stevanovic, M. Yang, K. Zhu and J. J. Berry, "Defect Tolerance in Methylammonium Lead Triiodide Perovskite," *ACS Energy Lett. ,* vol. 1, pp. 360-366, 2016.

[31] A. Walsh, D. O. Scanlon, S. Chen, X. G. Gong and S. -H. Wei, "Self-Regulation Mechanism for Charged Point Defects in Hybrid Halide Perovskites," *Angew. Chem., Int. Ed.,* vol. 54, pp. 1791-1794, 2015.

[32] C. Eames, J. M. Frost, P. R. F. Barnes, B. C. O'Regan, A. Walsh and M. S. Islam, "Ionic transport in hybrid lead iodide perovskite solar cells," *Nat Commun . ,* vol. 24, no. 6, p. 7497, 2015.

[33] H. J. Snaith, A. Abate, J. M. Ball, G. E. Eperon, T. Leijtens, N. [. K. Noel, S. D. Stranks, J. T.-W. Wang, K. Wojciechowski and W. Zhang, "Anomalous Hysteresis in Perovskite Solar Cells," *J. Phys. Chem. Lett.,* vol. 5, pp. 1511-1515, 2014.

[34] X. Lian, L. Zuo, B. Chen, B. Li, H. Wu, S. Shan, L. X. Wu, L. Zuo, B. Chen, B. Li, H. Wu, S. Shan, G. Wu, X. Yu, C. Q., L. Chen, D. Yang, D. Cahen and H. Chen, "Light-induced beneficial ion accumulation for high-performance quasi-2D perovskite solar cells.," *Energy Environ. Sci.,* vol. 15, pp. 2499-2507, 2022.

[35] P. Lopez-Varo, J. A. Jiménez-Tejada, M. García-Rosell, S. Ravishankar, G. Garcia-Belmonte, J. Bisquert and O. Almora, "Device Physics of Hybrid Perovskite Solar cells: Theory and Experiment," *Advanced Energy Materials,* vol. 8, no. 14, p. 1702772, 2018.

[36] J. Thiesbrummel, S. Shah, E. Gutierrez-Partida, F. Zu, F. Peña-Camargo, S. Zeiske, J. Diekmann, F. Ye, P. K. Peters, K. O. Brinkmann, P. Caprioglio, A. Dasgupta, S. Seo, F. A. Adeleye, J. Warby, Q. Jeangros, F. Lang, S. Zhang, S. Albrecht and T. Riedl, "Ion-induced field screening as a dominant factor in perovskite solar cell operational stability," *Nature Energy,* Vols.

10.1038/s41560-024-01487-w, 2024.

[37] O.Hentz, P. Rekemeyer and S. Gradečak, *Adv. energy mat.,* vol. 8, no. 18, p. 1701378, 2018.

[38] A. Guerrero, J. Bisquert and G. Garcia-Belmonte, "Impedance Spectroscopy of Metal Halide Perovskite Solar Cells from the Perspective of Equivalent Circuits," *Chem. Rev.,* vol. 121, p. 14430−14484, 2021.

[39] A. C. Lazanas and M. I. Prodomidis, "Electrochemical Impedance Spectroscopy-A Tutorial," *ACS Meas. Sci. Au,* vol. 3, pp. 162-193, 2023.

[40] E. v. Hoff and D. Klotz, "Impedance spectroscopy for perovskite solar cells: characterisation, analysis, and diagnosis," *Journal of Material Chemistry C,* vol. 10, pp. 742-761, 2022.

[41] M. H. Futscher, M. J. Lee, L. McGovern, L. A. Muscarella, T. Wang, M. I. Haider, A. Fakharuddin, L. Schmidt-Mende and B. Ehrler, "Quanti- fication of ion migration in CH3NH3PbI3 perovskite solar cells by tran- sient capacitance measurements.," *Mater. Horiz.,* vol. 6, p. 1497 1503, 2019.

[42] O. Almora, C. Aranda, E. Mas-Marzá and G. Garcia-Belmonte, "On Mott-Schottky analysis interpretation of capacitance measurements in organometal perovskite solar cells.," *Applied Physics Letters,* vol. 109, 2016.

[43] M. Fischer, T. Kristofer , A. Baumann and V. Dyakonov, "Doping Profile in Planar Hybrid Perovskite Solar Cells Identifying Mobile Ions," *ACS Applied Energy Materials,* 2018.

[44] C. Dindault, H. Jun, D. Tondelier, B. Geffroy, J.-E. Bourée, Y. Bonnassieux, P. Schulz and S. Swaraj, "Metal halide perovskite layers studied by scanning transmission X-ray microscopy," *RSC Advances,* vol. 12, p. 25570, 2022.

[45] H. Jun, H. R. Lee, D. Tondelier, B. Geffroy, P. Schulz, J.-E. Bourée, Y. Bonnassieux and S. Swaraj, "Soft X-ray characterization of halide perovskite film by scanning transmission X-ray microscopy," *Scientific Reports,* no. 12, p. 4520, 2022.

[46] H. Jun, C. Dindault, D. Tondelier, B. Geffroy, I. Florea, J.-E. Bourée, P. Schulz, Y. Bonnassieux and S. Swaraj, "On the use of soft X-ray STXM for organic-inorganic halide perovskite photovoltaic materials," *Journal of Electron Spectroscopy and Related Phenomena,* vol. 266, p. 147358, 2023.

[47] N. J. Jeon, J. H. Noh, Y. C. Kim, W. S. Yang, S. Ryu and S. Seok, "Solvent engineering for high-performance inorganic-organic hybrid perovskite solar cells.," *Nature Materials,* vol. 13, pp. 897-903, 2014.

[48] K. Liang, D. B. Mitzi and M. T. Prikas, "Synthesis and characterization of organic− inorganic perovskite thin films prepared using a versatile two-step dipping technique," *Chemistry of Materials,* vol. 10, no. 1, pp. 403-411, 1998.

[49] B. Dongqin, S. J. Moon, L. Haggman, G. Boschloo, L. Yang, E. M. J. Johansson, M. K. Nazeeruddin, M. Gratzel and A. Hagfeldt, "Using a two-step deposition technique to prepare perovskite (CH3NH3PbI3) for thin film solar cells based on ZrO2 and TiO2 mesostructures," *RSC Advances,* vol. 3, no. 41, pp. 18762-18766, 2013.

[50] A. Mei, X. Li, I. Liu, Z. Ku, T. Liu, Y. Rong, M. Xu, M. Hu, J. Chen, Y. Yang, M. Gratzel and H. Han, "A hole-conductor-free, fully printable mesoscopic perovskite solar cell with high stability," *Science,* vol. 345, no. 6194, p. 295–298, 2014.

[51] N. Ahn, D.-Y. Son, Y. H. Jang, S. M. Kang, M. Choi and N.-G. Park, "Highly Reproducible Perovskite Solar Cells with Average Efficiency of 18.3% and Best Efficiency of 19.7% Fabricated via Lewis Base Adduct of Lead(II) Iodide," *J. Am. Chem. Soc.,* vol. 137, no. 27, p. 8696–8699, 2015.

[52] T. Abzieher and D. T. Moore, "Vapor Phase Deposition of Perovskite Photovoltaics: Short Track to Commercialization?," *Energy Environ. Sci.,* vol. 17, pp. 1645-1663, 2024.

[53] R. Belkhou, S. Stanescu, S. Swaraj, A. Besson, M. Ledoux, M. Hajlaoui and D. Dalle, "A Soft X-Ray Beamline Dedicated to X-Ray Microscopy," *J Synchrotron Rad,* vol. 22, no. 4, p. 968–979, 2015.

[54] G. Richardson, S. E. J. O'Kane, R. G. Niemann, T. A. Peltola and P. J. Cameron, "Can slow-moving ions explain hysteresis in the current-voltage curves of perovskite solar cells?," *Energy Environ. Sci.,* vol. 9, no. 4, p. 1476–1485, 2016.

[55] J. S. Yun, J. Seidel, J. Kim, A. M. Soufiani, S. Huang, J. Lau, N. J. Jeon, S. I. Seok, M. A. Green and A. Ho-Baillie, "Critical role of grain boundaries for ion migration in formamidinium and methylammonium lead halide perovskite solar cells," *Adv. Energy Mater.,* vol. 6, no. 13, pp. 1-8, 2016.

[56] A. Senocrate, I. Moudrakovski, G. Y. Kim, T.-Y. Yang, G. Gregori, M. Grätzel and J. Maier, "The nature of ion conduction in methylammonium lead iodide: A multimethod approach," *Angew. Chemie- Int. Ed,* vol. 56, no. 27, p. 7755–7759, 2017.

[57] J. M. Frost, K. T. Butler and A. Walsh, "Molecular ferroelectric contributions to anomalous hysteresis in hybrid perovskite solar cells," *APL Mater.,* vol. 2, no. 8, 2014.

[58] C. Aranda, J. Bisquert and A. Guerrero, "Impedance spectroscopy of perovskite/contact interface: Beneficial chemical reactivity effect," *J. Chem. Phys.,* vol. 151, no. 12, 2019.

[59] J. N. Wilson, J. M. Frost, S. K. Wallace and A. Walsh, "Dielectric and ferroic properties of metal halide perovskites," *APL Mater.,* vol. 7, no. 1, 2019.

[60] J. P. Correa Baena, L. Steier, W. Tress, M. Saliba, S. Neutzner, T. Matsui, F. Giordano, T. J. Jacobsonn, A. R. S. Kandada, S. M. Zakeeruddin, A. Petrozza, A. Abate, M. K. Nazeeruddin, M. Grätzel and A. Hagfeldt, "Highly efficient planar perovskite solar cells through band alignment engineering," *Energy and environmental science,* vol. 10, no. 25, 2015.

[61] C. Aranda, J. Bisquert and A. Guerrero, "Impedance spectroscopy of perovskite/contact interface: Beneficial chemical reactivity effect," *J. Chem. Phys.,* vol. 151, no. 12, 2019.

[62] W. Tress, N. Marinova, T. Moehl, S. M. Zakeeruddin, M. K. Nazeeruddin and M. Grätzel, "Understanding the rate-dependent J-V hysteresis, slow time component, and aging in CH3NH3PbI3 perovskite solar cells: The role of a compensated electric field," *Energy Environ. Sci.,* vol. 8, no. 3, p. 995–1004, 2015.

[63] C. Li, S. Tscheuschner, F. Paulus, P. E. Hopkinson, J. Kießling, A. Köhler, Y. Vaynzof and S. Huettner, "Iodine Migration and its Effect on Hysteresis in Perovskite Solar Cells," *Advanced Materials,* vol. 28, no. 12, p. 2446–2454, 2016.

[64] C. Li, A. Guerrero , Y. Zhong, A. Gräser, C. A. Melo Luno, J. Köhler, J. Bisquert, R. Hildner and S. Heuttner, "Real-Time Observation of Iodide Ion Migration in Methylammonium Lead Halide Perovskites," *Small,* vol. 13, no. 42, p. 1–10, 2017.

[65] O. Almora, P. Lopez-Varo, R. Escalante, J. Mohanraj, L. F. Marcel, S. Olthof and J. A. Anta, "Instability analysis of perovskite solar cells via short-circuit impedance spectroscopy: A case study on NiOx passivation," *Journal of Applied Physics,* vol. 136, no. 9, p. 094502, 2024.

[66] W. Clarke, G. Richerdson and P. Cameroon, "Understanding the Full Zoo of Perovskite Solar Cell Impedance Spectra with the Standard Drift-Diffusion Model," *Advanced Energy Materials,* vol. 14, no. 32, p. 2400955, 2024.

Supporting Information

1- PSCs device preparation

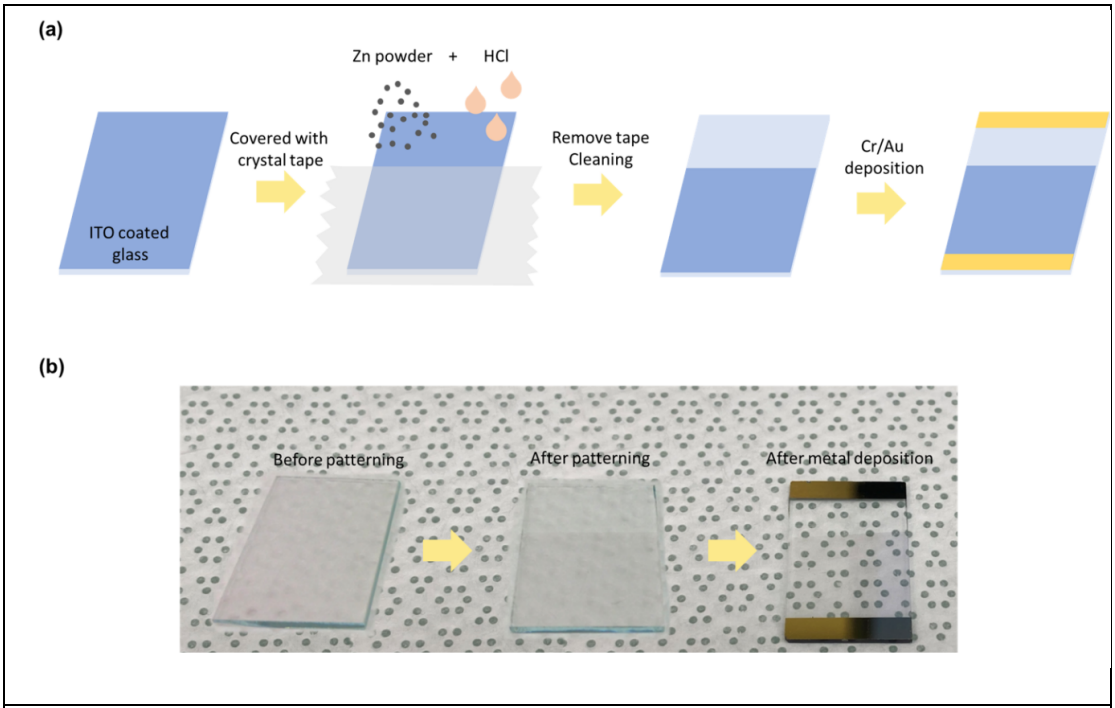

Figure S1 (a) Illustration of ITO etching and Cr/Au deposition process for the substrate of solar cells. (b) Real image of ITO-coated glass before and after patterning, completed substrate with Cr/Au contact.

Substrate with anode: Prior to the fabrication of PSCs, patterned Indium Tin Oxide (ITO) was etched using a wet process and employed as both the anode and substrate. Figure S1 illustrates the chemical etching and metal deposition procedures for substrate preparation. Initially, areas of ITO-coated glass substrates (20ohm/sq, Xinyan Technologies) requiring protection during etching were covered with 3M crystal clear tape. The exposed ITO was then removed using a solution of hydrochloric acid (HCl) and zinc powder (Zn). Subsequently, the etched substrate underwent cleaning in ultrasonic baths of deionized water with 1% diluted detergent (Liqui-Nox Phosphate-Free Liquid Detergent, Alconox, Inc.) for 15 minutes, followed by pure deionized water for 30 minutes, acetone for 15 minutes, and 2-propanol (IPA) for 15 minutes, in that order. To decrease the contact resistance between ITO and the measurement system,

chromium (Cr) and gold (Au) were thermally evaporated onto the glass-ITO edge (Figure IS1(a)) under a vacuum of 1×10^{-6} mbar. Specifically, a 5 nm layer of Cr was utilized to enhance adhesion between the glass and Au.

Hole transport layer (HTL): PEDOT:PSS was used as HTL. The surface of patterned ITO was treated with a UV-ozone chamber for 15 minutes. PEDOT:PSS solution (AI 4083, Ossila) was filtered through a 0.45 μm PVDF filter and deposited on UV-ozone activated ITO layer through spin-coating in air. Meanwhile, poly(styrene sulfonate) (PSS) in PEDOT:PSS is used as the counter ion and charge compensator which makes PEDOT:PSS easily dispersible in water. 120 μL of methanol was dropped during spin-coating of PEDOT:PSS to improve its conductivity [D. Alemu, H. Y. Wei, K. C. Ho and C. W. Chu, *Energy Environ. Sci,* vol. 5, no. 11, pp. 9662-9671, 2012.] This was followed by thermal treatment at 120°C in air for 20 minutes. The thickness of HTL layer is 25 nm.

Methyl ammonium lead iodide (MAPbI3): MAI (>99.99 %, Greatcell Solar Materials) and PbI_2 (ultra-dry, 99.999% Sigma Aldrich) precursors in crucibles are heated leading to sublimation. A pre-calibrated quartz crystal microbalance (QCM) sensor was used to monitor the rate of two precursors and the thickness of $MAPbI_3$. PbI_2 and MAI was sublimated in the vacuum chamber at 300 ℃ and 180 ℃, with the deposition rate of 1 Å/s and 2.5 Å/s, respectively. During evaporation, the vacuum level was 5.5×10^{-5} mbar. After deposition, the film was annealed at 70 °C for 10 min in an N_2-filled glove box. The optimal thickness for the PSC is 500 nm. For samples prepared for STXM in-situ biasing measurements a shadow mask was placed on a specially designed biasing chip to expose a zone on and between the electrodes for deposition through evaporation.

Electron transport layer (ETL): Thin films of C_{60}, from Ossila (99.5 %, CAS: 99685-96-8), was deposited on MAPbI3 by thermal evaporation as an ETL. The vacuum chamber was evacuated to a pressure of 7.6×10^{-7} mbar. C_{60} was sublimated at 500 ℃ with a deposition rate of 0.1 Å/s with a thickness of 25 nm.

Hole blocking layer (HBL): BCP was used for HBL to enhance charge separation and avoid the recombination of charges. BCP was also deposited on C_{60} by thermal vapor deposition. The vacuum conditions were same as those of C_{60} deposition. BCP (> 99.5 %, Lumtech, CAS: 4733-39-5) was sublimated at 100 ℃ with deposition rate of 0.1-0.2 Å/s with a thickness of 8 nm.

Cathode Silver (Ag) of 120 nm thickness was deposited for a cathode under a vacuum

of 1×10^{-6} mbar.

2. Circuit models used for data fitting according to Nyquist plot

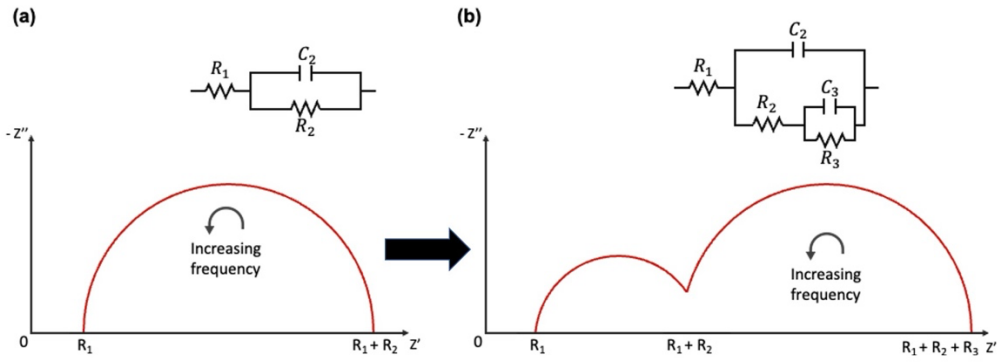

Figure S2: The circuit models used for data fitting according to Nyquist plot a) single arc case and b) double arc case.

3. Power conversion efficiency (PCE), hysteresis index (HI) and statistical histogram

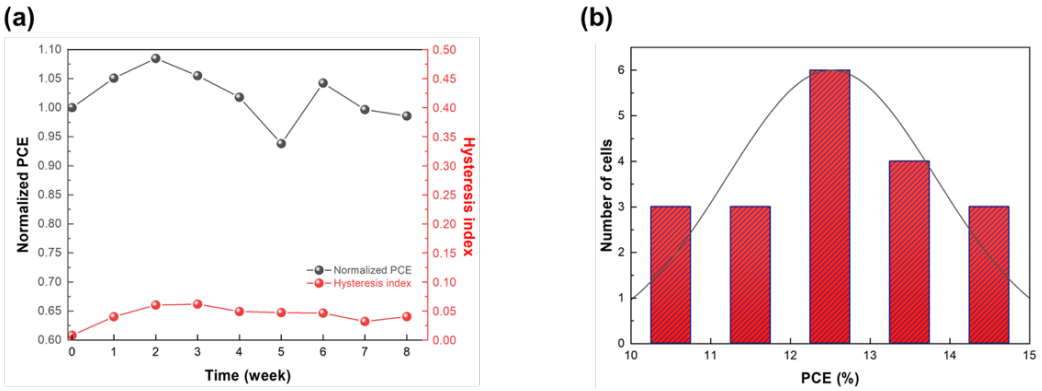

Figure S3: (a) PCE and hysteresis index of perovskite solar cell stored in N_2 and under dark as a function of time, (b) statistical histogram of PCE of 19 individual devices.

4. Schematic of the energy diagram of the different layers of the analyzed PSC C_{60}/MAPI/PEDOT:PSS

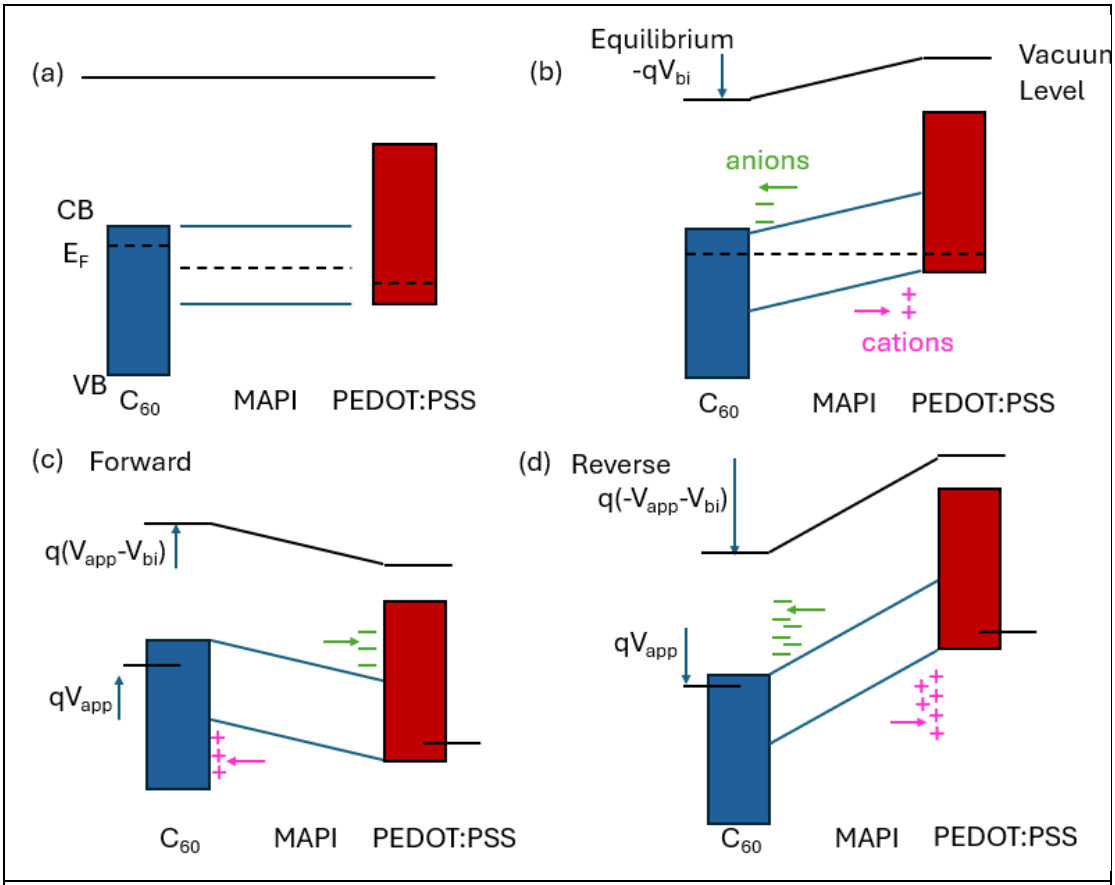

Figure S4 (a), (b) Schematic of the energy diagram of the different layers of the analyzed PSC C_{60}/MAPI/PEDOT:PSS before and after being on contact. CB, VB and EF are the conduction band, valence band and Fermi level, respectively. Vbi is the built-in potential created by the difference of the work functions of the HTL (PEDOT:PSS) and ETL (C_{60}). (c) and (d) represent the energy diagram once forward and reverse bias have been applied. Vapp is the applied voltage. The migration of ions according to the electric field is indicated by arrows. The schematics does take into account the band bending due to ions on the perovskite layer.

5. Analysis of ESI results before and after applied electric field under dark conditions

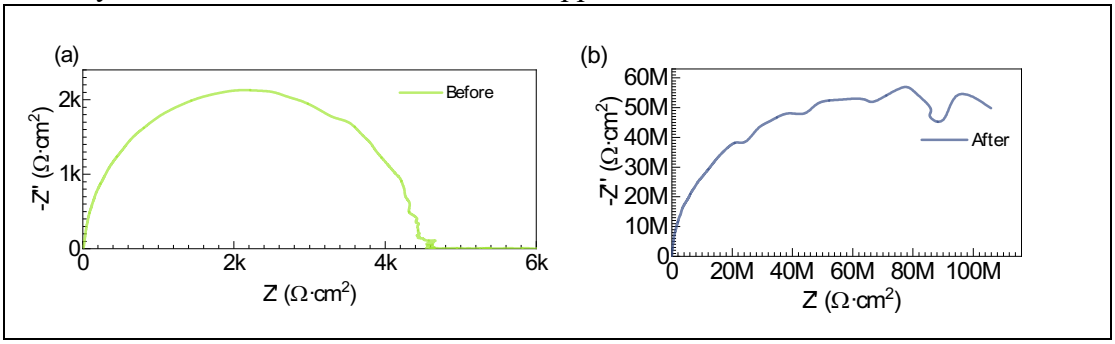

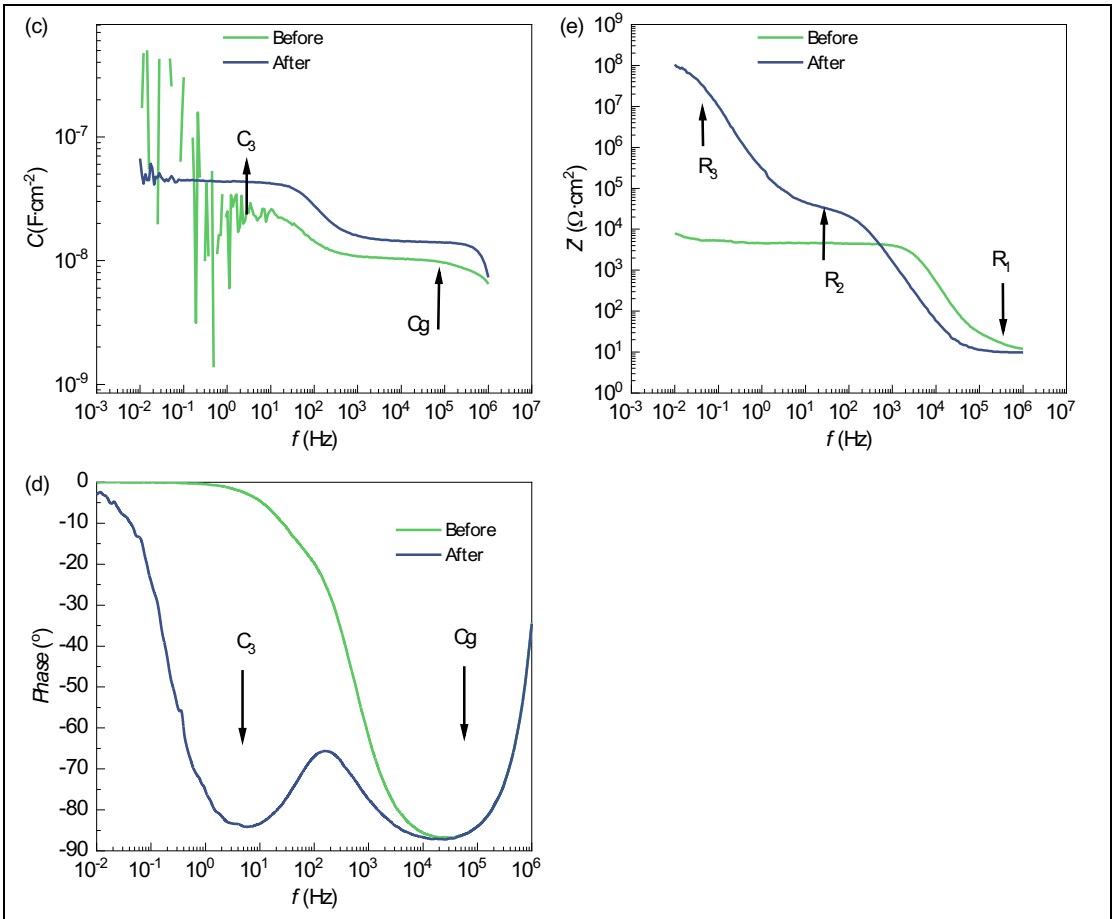

Figure S5. (a) and (b) Nyquist of the impedance of $MAPbI_3$ before and after applied electric field under dark conditions, respectively. (b), (c) and (d) Capacitance, real part of the impedance -resistance- and phase extracted from the total impedance.

6. Analysis of ESI results as a function of ageing time

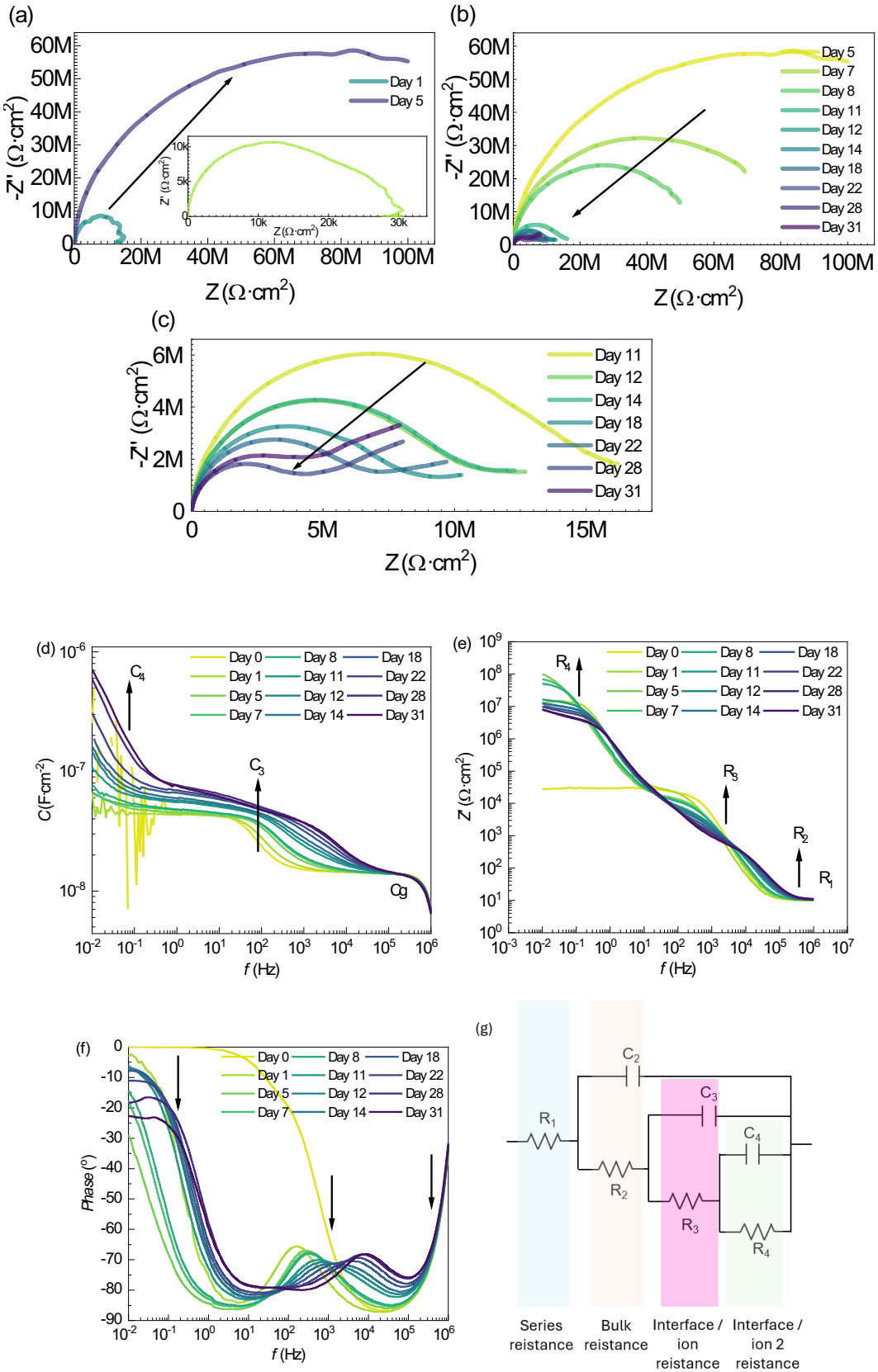

Figure S6. (a), (b) and (c) Nyquist of the impedance of $MAPbI_3$ during the ageing test measured under dark conditions. (d), (e) and (f) Capacitance, real part of the impedance -resistance- and phase extracted from the total impedance. (g) circuital model to fit the

experimental data and the relation of each element RC with a physical phenomenon.

Impedance Spectroscopy basic equations:

In an IS measurement, a small-signal, sinusoidal electrical input signal (V_{AC}) is added on the applied DC voltage (V_{DC}) [J. Mater.Chem. C, 2022, 10, 742-761]:

$$V(\omega t) = V_{DC} + V_{AC} = V_{DC} + V_0 \sin(\omega t) \quad \text{(Eq. S1)}$$

where $\omega = 2\pi f$ is the angular frequency. The resulting alternating current (I_{AC}) is measured and is given by:

$$I(\omega t) = I_{DC} + I_{AC} = I_{DC} + I_0 \sin(\omega t + \varphi) \quad \text{(Eq. S2)}$$

where φ represents the difference in phase angle between the input voltage V_{AC} and output current I_{AC} in the frequency domain.

The impedance Z is a transfer function that relates the input V_{AC} to the output I_{AC} via:

$$Z(\omega t) = \frac{V_0}{I_0} \exp(-i\varphi) = Z_0(\cos(\varphi) - i\sin(\varphi)) = Z' - iZ'' \quad \text{(Eq. S3)}$$

The impedance Z is a complex function that can be expressed by its magnitude-module (Z_0) and phase angle (φ) for each value of frequency ω:

$$Z_0 = |Z| = \sqrt{Z'^2 + Z''^2} \quad \text{(Eq. S4)}$$

$$\varphi = \tan^{-1}\left(\frac{-Z''}{Z}\right) \quad \text{(Eq. S5)}$$

The capacitance can be calculated from the impedance according to:

$$C = \frac{1}{i\omega Z} \quad \text{(Eq. S6)}$$